FY 2022 DOCTRAL THESIS

Development of the Polarization Modulation Unit of LiteBIRD Low-Frequency Telescope for exploration of primordial gravitational waves

原始重力波探索を行う LiteBIRD 低周波望遠鏡の偏光変調器開発

Author Shinya Sugiyama

Supervisor Makoto S. Tashiro

Graduate School of Science and Engineering

Saitama University

September 12, 2022

Abstract

Cosmic Microwave Background (CMB) is the isotropic blackbody radiation with the temperature of 2.725 K as today. In modern Cosmology, the observation of the linear polarization of the CMB has received a lot of attention for the validation of inflation theories. Inflation scenarios proposed the models of an exponential expansion which would happen in the very early Universe. The rapid expansion had been expected to produce primordial gravitational waves, which can be the only communicator in the era when photons could not go straight. The primordial gravitational waves signal can be observed in the CMB polarization. The CMB polarization can be decomposed to two patterns, called E-mode and B-mode. The detection of this primordial B-mode proves the inflation theory. The next generation satellite, LiteBIRD, is one of the satellites which aims to observe this B-mode. LiteBIRD is the JAXA/ISAS strategic large class satellite mission and will observe full-sky from the second Lagrange point (L2). LiteBIRD employs three telescopes, Low-, Mid-, and High-Frequency Telescope (LFT/ MFT/HFT) in 15 frequency bands between 34 and 448 GHz. All telescopes adopt polarization modulation units (PMU), which are the instruments for rotating a half-wave plate (HWP) continuously, to reduce a $1/f$ noise and systemic effects from the difference of orthogonal detectors. The PMUs adopt a brush-less motor and a superconducting magnetic bearing to realize a contact-less rotation of the PMU rotor, which will implement a five stacking layer sapphire HWP. In our study, we evaluate the performances of the prototype of the LFT PMU of LiteBIRD. As the critical performance, we evaluate the reconstruction method and the results of position angles of the HWP. This HWP angle has a correspondence with the incident polarization angle which is used for the demodulation of observation signals. The accuracy of reconstructed angles can depends on a systematic effect which is a source of the leakage of E-mode into B-mode. Through the study shown in chapter 3, the accuracy is estimated as 2.48×10^{-1} arcmin, which satisfies the design guidance value of 0.5 arcmin. The potential sources of the error of position angles are investigated, and evaluated quantitatively. As a total, it is shown that the root mean square of all error components is consistent with the angular accuracy due to the measured periods. In addition to the above uncertainty of rotation angle, vibration of the PMU rotor could be potential sources of noises. The PMU equipped with the non-contact

rotation could be suffered from vertical vibration. Chapter 4 describes a measurement of the vertical displacement of the PMU rotor with a Hall sensor and a capacitive sensor in stable rotation at 1 Hz to show the displacement of the PMU rotor becomes 36 μm. According to this displacement, two expected effects due to the vibration of the PMU rotor are evaluated, and forecast the potential impact on the low-temperature detector system is discussed in chapter 5.

Contents

List of Figures

List of Tables

Chapter 1.

Introduction

1.1 Cosmic Microwave Background (CMB) and Standard Cosmology

Big-Bang model is the model that predicts the early Universe was hotter and more dense than the current Universe, supposed by (19; 20) in the 1940s. This model predicted the expanding Universe from the point of the view of elements origin. Also, this model predicted the temperature of radiations, $\sim$5 K, which is the remnants of the hot and dense Universe in the past.

Detection of the CMB

The predicted radiations are currently called the Cosmic Microwave Background (CMB). The CMB was coincidentally discovered by an experiment shown in (21). A purpose of this experiment was the measurement of an intensity of Cassiopeia A, which is one of radio astronomical objects. The observation was done by horn antenna, which had a 6 m × 6 m aperture as shown in Figure 1.1, in Bell laboratories in Holmdel, NJ, in USA. The horn antenna could cancel the detector noise by measuring the sky temperature and the cold load (5K). As the result, there was 3.5 K of the excess temperature component, which can not be explained by signals from sky, any systematic effects, and detector noise. This excess temperature could be observed in full sky, consistent with the prediction of Big-Bang model, and finally concluded as the CMB. After this first detection, several following instruments have observed the CMB.
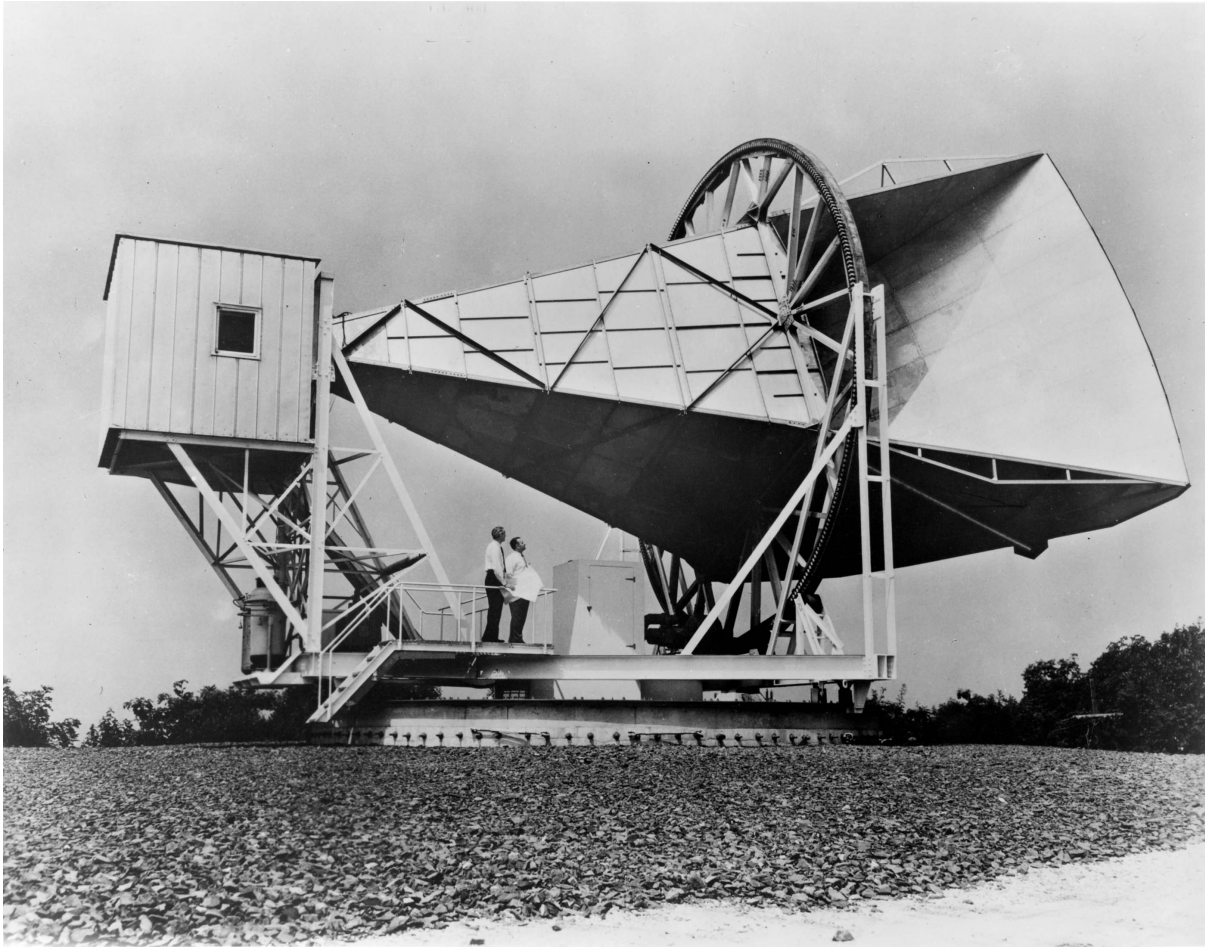
Figure1.1   Horn antenna used in Bell laboratories (1)

Discovery of the CMB anisotropy

In 1989, NASA launched a space telescope called Cosmic Background Explorer (COBE) (22; 23). COBE enables the observation in full sky at $7°$ field of view, and without contributions of the Earth atmosphere. COBE had three scientific telescope; the differential microwave radiometer (DMR), the far-infrared absolute spectrophotometer (FIRAS), and the diffuse infrared background experiment (DIBRE). Especially, the DMR instrument is used for a precise full-sky observation at the scale of 10^{-5} K. And the FIRAS instrument is used for the spectrum of the CMB in the wavelength from 100 μm to 1 cm. The COBE observation showed the full-sky CMB temperature map (Figure 1.2) has the anisotropy (24; 25; 26). This is due to an inhomogenities of matter distribution in the early Universe. Additionally, the CMB intensity spectrum has a good agreement with a
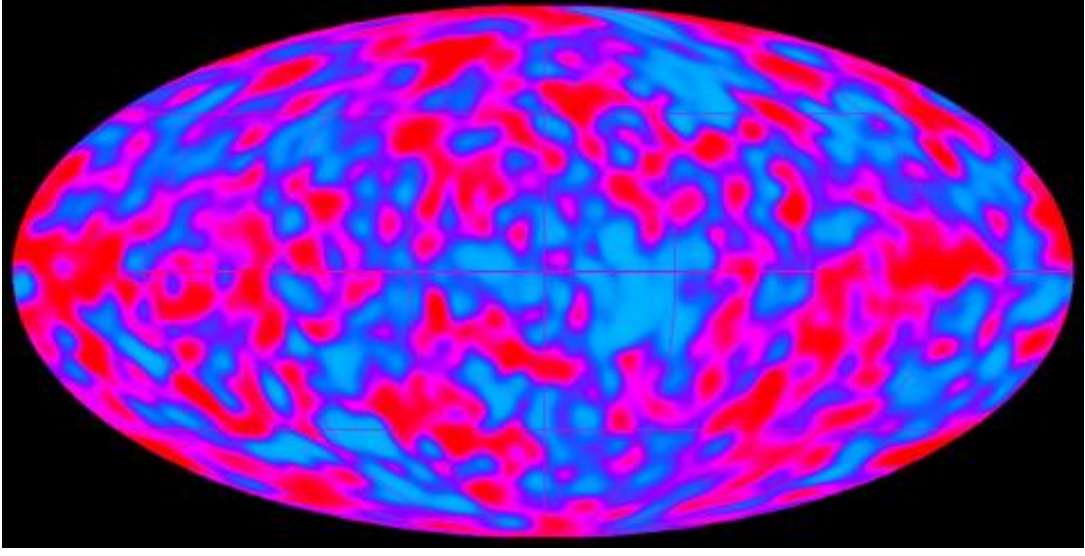
Figure1.2 The full-sky temperature map by the CMB observation of COBE (2).

theoretical spectrum of blackbody at 2.725 K. This is the proof that there was a thermal equilibrium between matters and radiations at the early Universe. Finally, all observation results supported the Big-Bang model.

Cosmological parameters and Λ Cold Dark Matter Model

In 2001, NASA launched the CMB observation satellite, called Wilkinson Microwave Anisotropy Probe (WMAP) (27; 5; 28; 29). Compared with the angular resolution of COBE, $7°$, WMAP has the higher angular resolution, $0.2°$. The full-sky map from WMAP is shown as Figure 1.4. This map can be disassembled as powers at a multipole moment, ℓ, by using a spherical harmonic expansion, which can be shown as

$$T(\theta, \phi) = \sum_{\ell m} a_{\ell m} Y_{\ell m}(\theta, \phi),$$

(1.1)

where θ and ϕ are positions in spherical coordinates, $a_{\ell m}$ is expansion coefficients, and $Y_{\ell,m}(\theta, \phi)$ are the ℓ-order spherical harmonic functions. By using the $a_{\ell m}$, the spectrum C_ℓ on the angular scale of the CMB temperature anisotropy can be shown as

$$C_\ell \equiv \frac{1}{2\ell + 1} \sum_{m=-\ell}^{\ell} a_{\ell m} a_{\ell m}^*.$$

(1.2)

The angular power spectrum of the observed temperature map from WMAP is shown in Figure 1.5. The results of WMAP enables to utilize the smaller scale structure ($\ell \sim 1000$)
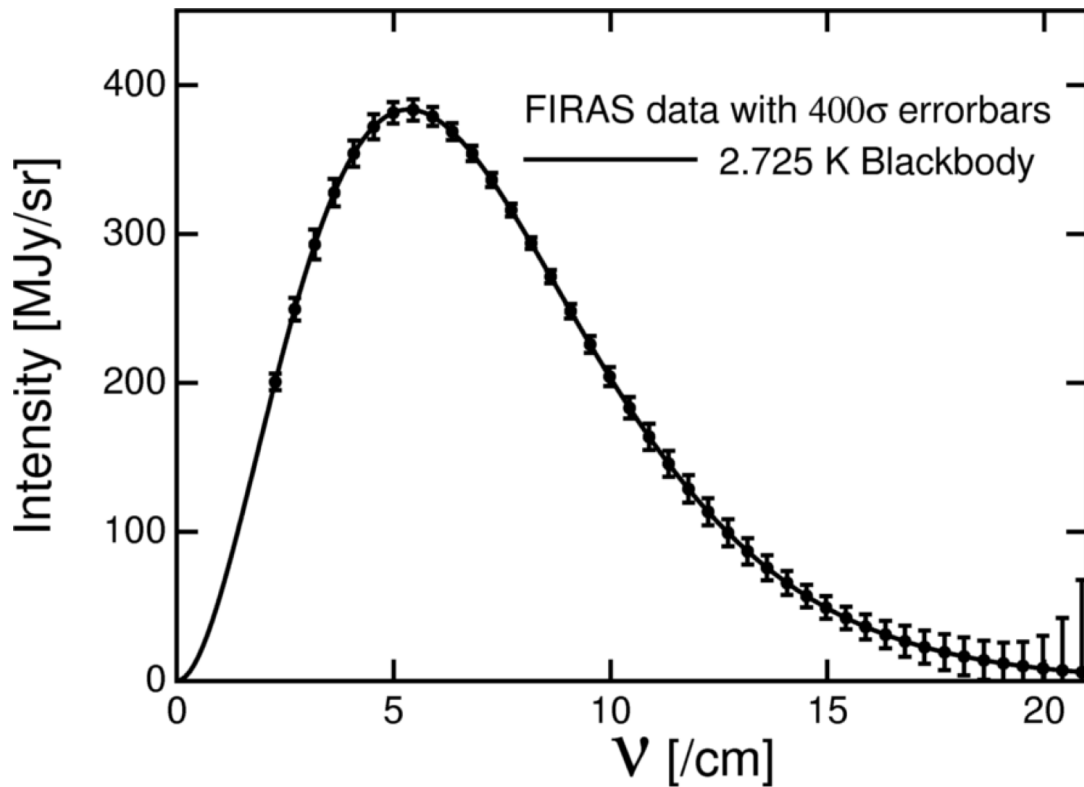
Figure1.3   The spectrum of the CMB intensity measured by the COBE FIRAS and the theoretical spectrum of blackbody at 2.725 K (3; 4).
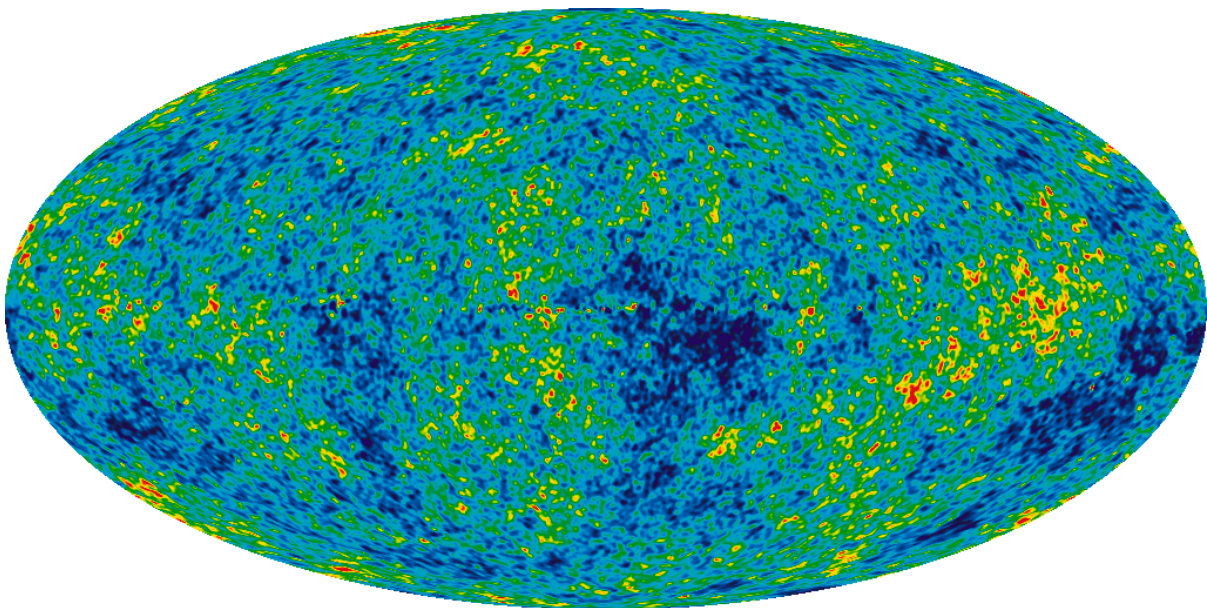
Figure1.4   The full-sky temperature map by the CMB observation of WMAP (5).
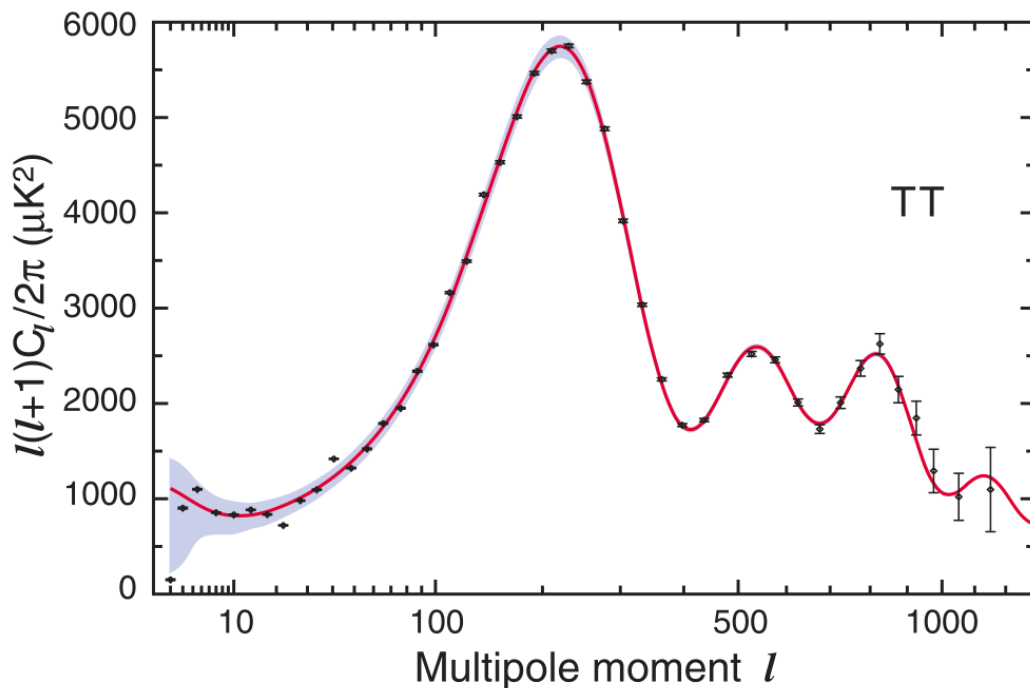
Figure1.5   The power spectrum from the CMB temperature anisotropy from WMAP (5).

compared with the results of COBE ($\ell < 20$). The model of this power spectrum consists of cosmological parameters, which are the basis of standard model of the Universe, so called Λ Cold Dark Matter (ΛCDM) model. The fitting of the power spectrum from WMAP reveals the cosmological parameters. The best fitting parameters are decided with $\sim 1\%$ precision.

CMB measurement with further high sensitivity

The following CMB space telescope, *Planck*, also observed the anisotropic of the CMB temperature and the pattern of CMB polarization (6). *Planck* was launched in 2009, and has observed the full sky with high frequency instrument (HFI) and low frequency instrument (LFI) until 2013. The observation frequency range was covered as nine bands from 30 to 857 GHz by using both instruments. And the instruments have sub-Jansky sensitivities and the higher angular resolution < 10 arcmin. *Planck*'s observation achieved the measurement of almost cosmological parameters with better accuracy $< 1\%$. Figure 1.6 shows the full-sky map of the CMB temperature and polarization. The power spectrum of
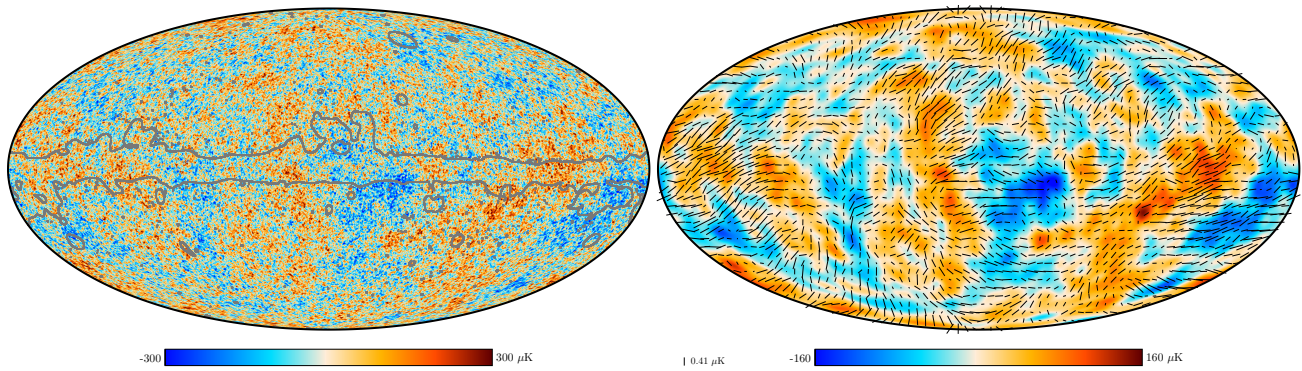
Figure1.6 The full-sky map of the CMB temperature and polarization from *Planck* observation (6; 7).

the temperature anisotropy is shown as the curve of CMB-TT in Figure 1.7. This power spectrum has the good agreement in all range of multipoles with the results of WMAP and the ground observation instruments, ACT (30) and SPTpol (31; 32).

1.2 Inflation theory and CMB polarization

As above, standard cosmological model was mainly established by CMB measurement results. This model can describe the status of current Universe, on the other hand, this includes unsolved problems; horizon problem, flatness problem, magnetic monopole problem, and the origin of the large scale structure. These are solved by the cosmic inflation theory which describe a scenario of an exponential expansion of the early Universe.

The cosmic inflation is a theoretical model which predicts an exponential cosmic expansion happened at the early Universe. According to the theory of the cosmic inflation, the origin of the inflation is from quantum fluctuations in the very early Universe, and which made the primordial fluctuations. After the inflation, the Universe was filled with a hot and dense plasma, and these are cooled by an accelerated expansion that continues today. Mechanisms and details of the cosmic inflation vary by the theoretical models, but the models predict the cosmic inflation generated a scalar mode (density perturbations) and a tensor mode (primordial gravitational waves). These perturbations are imprinted in the temperature and polarization anisotropies in the CMB photons at last scattering.
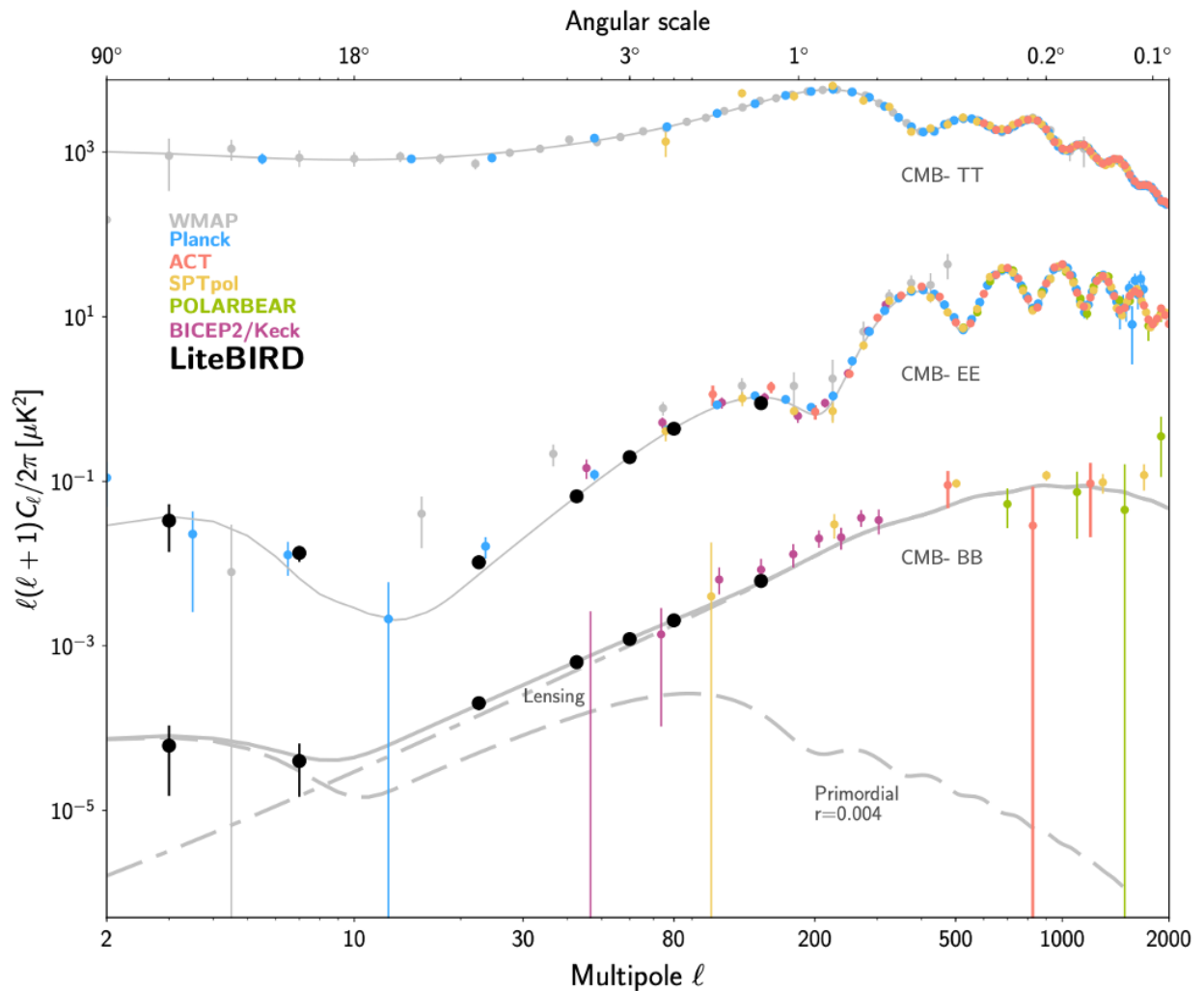
Figure1.7   The power spectrum of the CMB temperature anisotropy and polarization anisotropy (8).

Measurement of the CMB polarization

WMAP and *Planck* has observed the anisotropy of the CMB. The linear polarization is produced by Thomson scattering of photons by electrons and a quadrupole temperature anisotropy on the last scattering surface (see Figure 1.8). An information of the CMB linear polarization can be expressed as Stokes parameters, I, Q, and U. The parameters
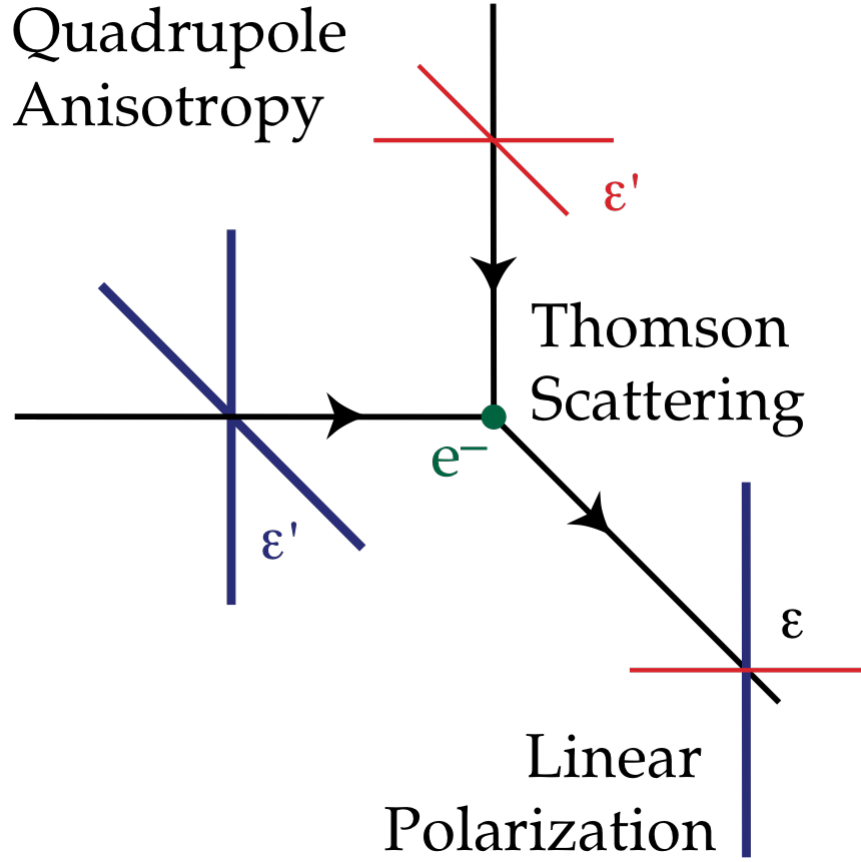
Figure1.8 A mechanism generating the linear polarization of the CMB (5).

are shown as

$$I \equiv \hat{E_0}^2 + \hat{E_{90}}^2, \tag{1.3}$$

$$Q \equiv \hat{E_0}^2 - \hat{E_{90}}^2, \tag{1.4}$$

$$U \equiv \hat{E_{45}}^2 - \hat{E_{-45}}^2, \tag{1.5}$$

where $\hat{E_0}$ and $\hat{E_{90}}$ are amplitudes of orthogonal electric fields of the CMB, and $\hat{E_{45}}$ and $\hat{E_{-45}}$ are ones of electric fields of the CMB with polarization axes rotated 45 ° and -45°. By using both parameters, a polarization intensity P and a polarization angle α can be shown as

$$P \equiv \sqrt{Q^2 + U^2}/I \tag{1.6}$$

$$2\alpha \equiv \arctan(U/Q). \tag{1.7}$$

The values of Stokes parameters depend on how a coordinate is defined. The Stokes parameters Q and U can be expanded as

$$[Q \pm iU](\theta, \phi) = \sum_{\ell m} {}_{\mp 2}a_{\ell m} {}_{\mp 2}Y_{\ell m}(\theta, \phi), \tag{1.8}$$

where ${}_{\mp 2}a_{\ell m}$ and ${}_{\mp 2}Y_{\ell m}$ are spin-2 expansion coefficients and spin-2 spherical harmonics. By using spin-2 expansion coefficients, the coordinate definition-independent expansion factors, $a_{\ell m}^E$ and $a_{\ell m}^B$ can be shown as

$$a_{\ell m}^E = -({}_2a_{\ell m} + {}_{-2}a_{\ell m})/2, \tag{1.9}$$
$$a_{\ell m}^B = i({}_2a_{\ell m} - {}_{-2}a_{\ell m})/2. \tag{1.10}$$

These parameters have no dependency in the definition of the coordinate, and each parameter is called E-mode and B-mode, respectively (33; 34; 35; 36). The E-mode is mainly caused due to the temperature (density) anisotropy. On the other hand, small E-mode and B-mode are caused by primordial gravitational waves predicted by an inflation of the Universe.

WMAP and *Planck* have observed the E-mode of the CMB polarization and lensing B-mode originated from the gravitational lensing effect. Especially, WMAP observed the E-mode in full sky at the first time (5). And *Planck* fulfilled the E-mode observation with the higher angular resolution, higher sensitivity, wider observation frequency range and lower noise than WMAP. Both power spectrum of WMAP and *Planck* are shown in Figure 1.7.

Additionally, several ground experiments and balloon experiments have also targeted the CMB polarization in this decade.

Validation of the cosmic inflation

If the inflation was in early Universe, there were primordial gravitational waves by the highly rapid expansion. In the duration between the inflation and the last scattering surface, photons cannot go straight by the frequent scattering with electrons. Then, primordial gravitational waves have stirred in the Universe during this period. As results, primordial gravitational waves engraves the special pattern of the CMB polarization, called primordial B-mode. The detection of this pattern is the crucial parameter for the validation of inflation scenario.

Lensing B-modes

The lensing B-mode is the E-mode twisted by the gravitational lensing effect. This B-mode is not related to the origin of the primordial B-mode. In the power spectrum, the peak of primordial B-modes is expected to be at large scales, $\ell \sim 100$. On the other hand, the peak of lensing B-mode is expected to be at $\ell \sim 1000$.

The fisrt detection of the lensing B-modes has been done by the ground experiment, South Pole Telescope (SPTpol), with the infrared observation map by the Hershel space observatory at 7.7σ significance (31). Additionally, the ground experiment, POLARBEAR and BICEP2, also detect the lensing B-modes, and showed its power spectrum (37; 38; 39; 40). Their observations revealed that the peak of lensing B-modes exists in the expected multipole, $\ell \sim 1000$, shown in Figure 1.7 (41).

The lensing B-modes are the foreground signal which has the different dependency in observation frequency from the primordial B-mode. Therefore, the multi-frequency observations enables the separation of these signals (42; 43; 6).

Detection of primordial B-modes?

Once the observation of BICEP2 showed the candidate of the power spectrum bump of primordial B-modes in 2014 (44; 39). The observation result of BICEP2 showed the excess bump, which is inconsistent with lensing B-modes, in the range $30 < \ell < 150$ with 3σ significance. This excess was hoped to be due to primordial gravitational waves, however, the excess bump could have the possibility due to the contribution of polarized dust emission. Therefore, the definitive proof of primordial B-modes has not been detected yet.

Scale invariance and tensor-to-scalar ratio

Planck also decided the index of power spectrum of the primordial fluctuation, called a scale invariance n_s, as 0.967 with less than 1 %.

And the primordial B-mode power depends on the tensor-to-scalar ratio, r. The major inflation models predict the value of $r > 0.01$ (45). The upper limit of r is limited by

observation results as < 0.036 (46).

The observation of primordial B-mode and the decision of r with high significance are the direct proof of the cosmic inflation, and there is the fierce competition to fulfill them by several experiment.

Chapter 2.

LiteBIRD

Next generation satellite, LiteBIRD, is one of the instruments which aim to detect the definitive proof of primordial B-modes (8; 10). The following sections introduces LiteBIRD from various perspectives.

2.1 Science goal

LiteBIRD aims to observe two bumps of the primordial B-mode power spectrum with higher significance. The power spectrum of the primordial B-mode is expected to have the bumps in $\ell \sim 10$, called the reionization bump, and in $\ell \sim 80$, called the recombination bump (47). The recombination bump is the prominent structure happened during the epoch for which the electrons and protons became the hydrogen atoms, and this epoch was neutral. The reionization bump is generated from the epoch for which the hydrogen atoms were ionizied by ultraviolet rays from first stars. There is the possibility that the ground-based observatory can detect reionization bump. On the other hand, the full sky survey of LiteBIRD has the possibility to detect both bumps.

However, the detection of both bumps in the B-mode power spectrum needs the unprecedented detector precision and control of all systematic effects. When the error of tensor-to-scalar ratio r is defined as δr, LiteBIRD aims to achieve $\delta r < 0.001$ to verify well-motivated inflation models that predict $r > 0.01$. δr consists of all uncertainties, such as instrumental systematics, in the observation of primordial B-mode.

2.2 Foreground removals

In the observation of the CMB temperature and polarization, the foreground emissions are one of major origins which generate systematic effects. Especially in the polarization measurement, there are two major origins of foreground emissions in radio band; electrons which move in a spiral motion in the Galactic magnetic field, and interstellar dusts aligned with the Galactic magnetic field. The electrons produce synchrotron emissions, which are dominant at lower frequency (< 80 GHz), and thermal dust emissions, which are dominant at higher frequency (> 80 GHz) (6).

Contributions of both foreground origins in the CMB polarization are measured by *Planck*, which shown in Figure 2.1. The intensity of the synchrotron radiation can be modeled as the power law,

$$I_\nu^s = A_s^I \left(\frac{\nu}{\nu_0^s} \right)^{\beta_s},$$

(2.1)

where ν is the observation frequency, A_s^I is the specific polarized intensity, ν_0^s is the pivot frequency, and β_s is the spectral index (48). On the other hand, the dust emission model is described as

$$I_\nu^d = A_d^I \left(\frac{\nu}{\nu_0^d} \right)^{\beta_d} B_\nu(T_d),$$

(2.2)

where A_s^I is the dimensionless amplitude, ν_0^d is the pivot frequency, β_d is the spectral index, and $B_\nu(T_d)$ is the Planck function at the temperature of the thermal dust, T_d (48). Both spectral indices, β_s and β_d, are determined as -3.1 ± 0.1 and 1.55 ± 0.05, respectively, by the results of *Planck* (49).

The frequency dependence of both foreground emissions differ from the CMB polarization significantly. For this separation, LiteBIRD observes full sky in 15 frequency bands from 34 GHz to 448 GHz. Thus, the multi-frequency bands observation of LiteBIRD allow us to distinguish the CMB signal from the foreground.
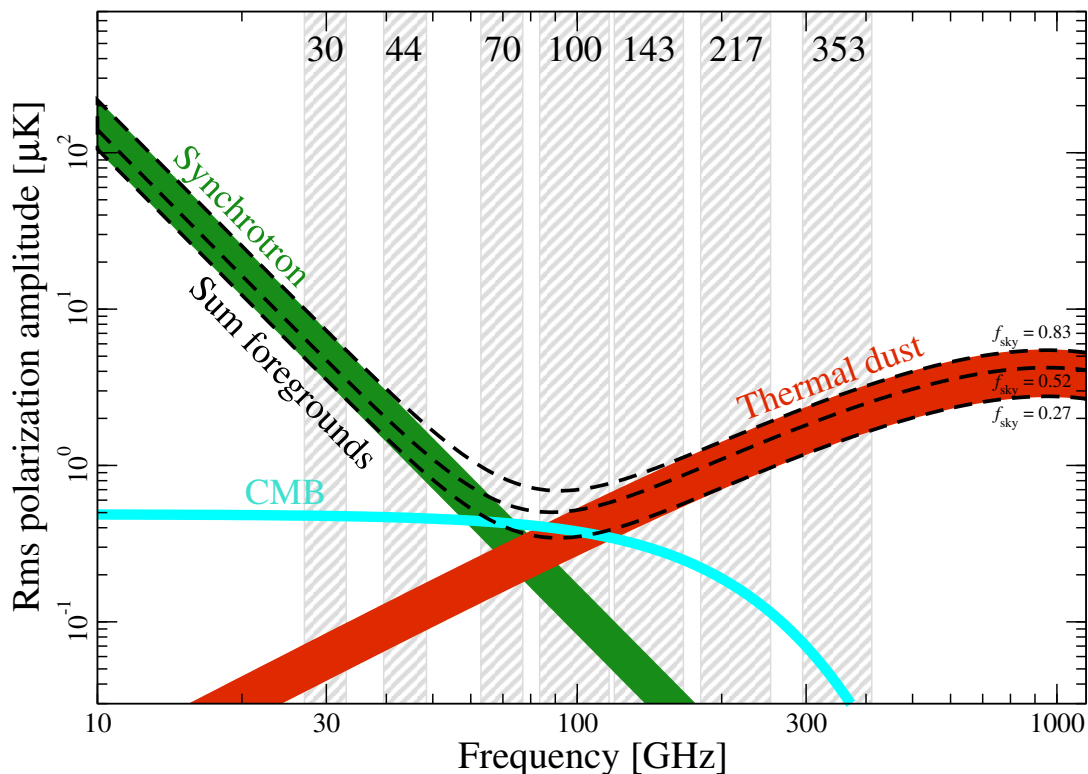
Figure2.1   The power spectrum of synchrotron emissions, thermal dust emissions, and the CMB polarization by the measurement of *Planck* (6; 7).

2.3 Mission overview

The summarized parameters of the mission overview of LiteBIRD are in Table 2.1. LiteBIRD will observe full sky to detect the primordial B-mode in lower multipoles (8). This satellite will be launched to Sun-Earth Lagrangian point, called L2, to avoid the effects of radiations from Sun, Moon, and Earth.

To prevent the detection of the sun light, LiteBIRD will adopt a sun shield and the payload module will observe the opposite direction anytime (see left panel of Figure 2.2). The operation will be carried out for three years. The precession cycle is ~3 hours with $45°$ tilted respect to the anti-sun direction, and the spin period is 20 min with $50°$ respect to the rotation axis of LiteBIRD (see right panel of Figure 2.2). In the payload module, there are three frequency range telescopes, called High/Mid/Low-Frequency Telescope (HFT, MFT, and LFT), shown as Figure 2.3.

Each telescope has also the detectors in subdivided frequency bands, shown in Table 2.2.
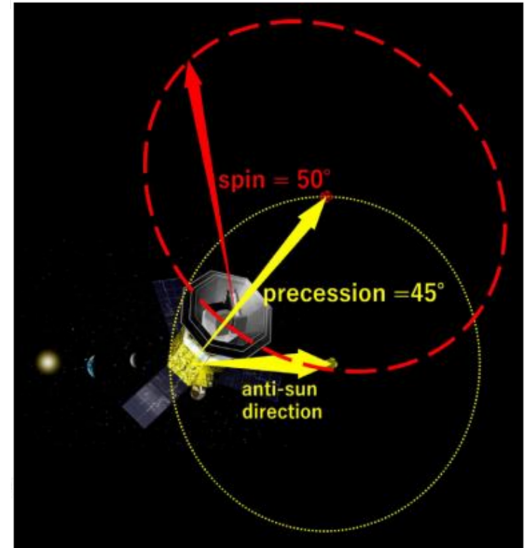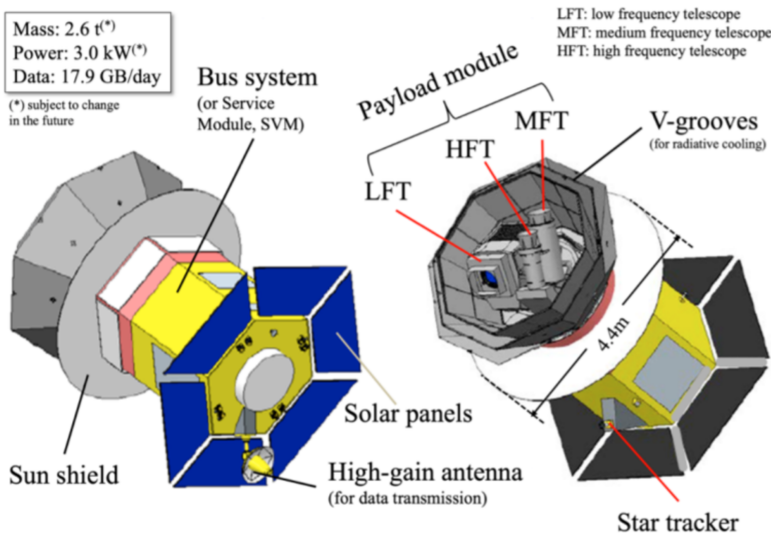
Figure2.2   Left: the overview model of LiteBIRD (8). Right: the Scans of LiteBIRD with 50° of spin angle and 45° of precession angle at L2 (9).
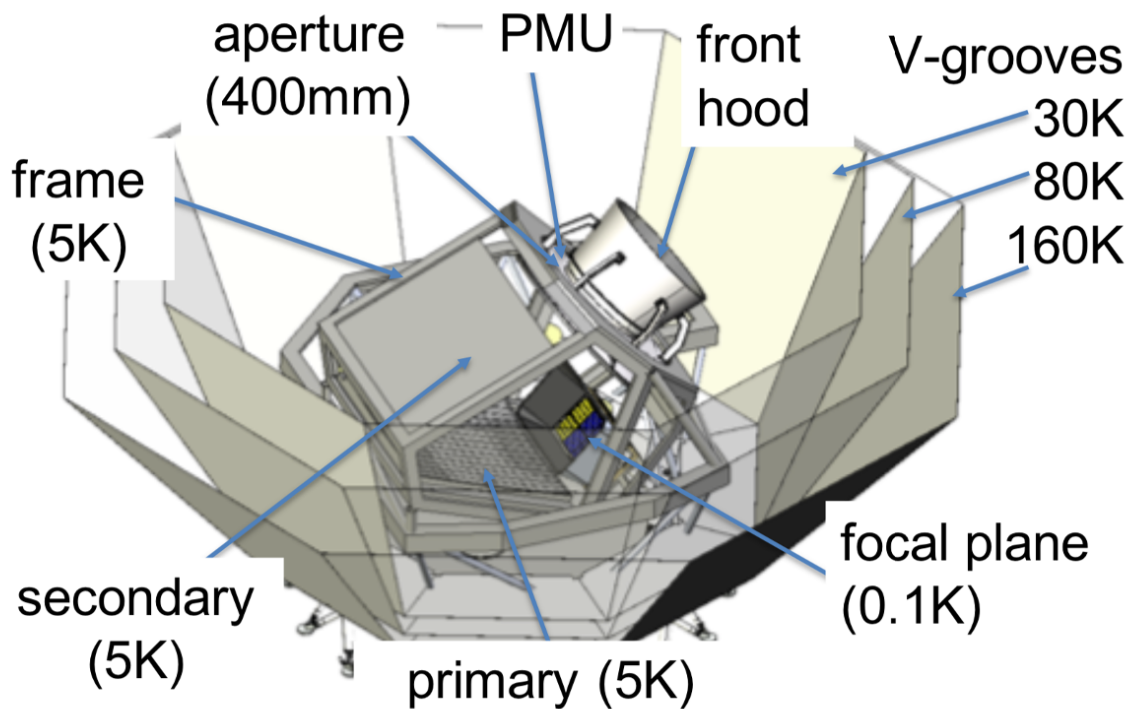
Figure2.3   The overview of payload modules in LiteBIRD (10).

Table2.1   Parameters of current baseline of LiteBIRD in the mission overview (9).

Launch schedule	2027 FY
Observation period	3 years
Target sensitivity of tensor-to-scalar ratio r	$\delta r < 0.001$
Target of multipole range	$2 \leq \ell \leq 200$
Orbit	Second Sun–Earth Lagrangian point L2; Lissajous orbit
Precession angle	$45°$
Precession rate	0.001 - 0.01 rpm
Spin angle	$50°$
Spin rate	0.05 - 0.1 rpm
Pointing knowledge	< 2.1 arcmin
Focal-plane detector	Multi-chroic superconducting detector arrays with more than 4000 TES bolometers
Sensitivity	2.0 μK·arcmin
Observing frequencies	15 bands between 34 and 448 GHz

Table2.2 The center frequency and the frequency band of LiteBIRD telescopes (10).

Telescope	Band ID	Center Frequency [GHz]	Frequency band [GHz] (Fraction)
LFT	1	40	12 (0.30)
LFT	2	50	15 (0.30)
LFT	3	60	14 (0.23)
LFT	4	68	16 (0.23)
LFT combined	5	78	18 (0.23)
LFT combined	6	89	20 (0.23)
LFT/MFT combined	7	100	23 (0.23)
LFT/MFT combined	8	119	36 (0.30)
LFT/MFT combined	9	140	42 (0.30)
MFT	10	166	50 (0.30)
MFT/HFT combined	11	195	59 (0.30)
HFT	12	235	71 (0.30)
HFT	13	280	84 (0.30)
HFT	14	337	101 (0.30)
HFT	15	402	92 (0.23)

2.4 Low-frequency telescope

LFT is mainly targeting on the CMB polarization and the synchrotron radiations to remove foreground contributions. The covered frequency range is from 34 GHz to 161 GHz divided by nine frequency bands, shown in Table 2.2. The internal structure of the optical
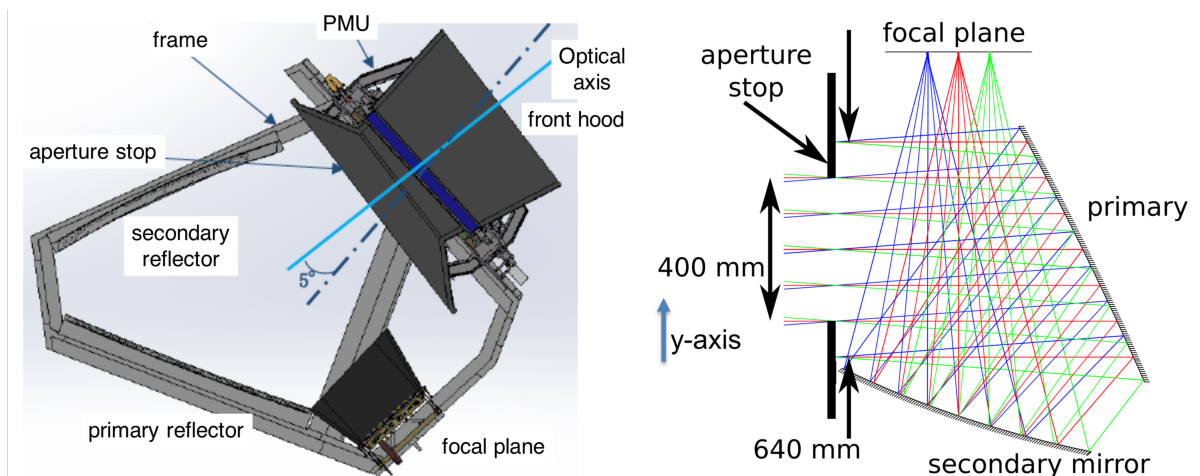
Figure2.4   Left: The overview of LFT in LiteBIRD. Right: A diagram of the tracking of rays in LFT. Both figures are from (10).

system is shown as Figure 2.4. In the entrance of the optical system, a polarization modulator unit (PMU) will be used, and which is explained in Section 2.5. The LFT adopts the crossed-Dragone optical system, which uses two mirrors to converge light on the focal plane. The configuration has the major advantage of the wide field-of-view ($18° \times 9°$). The focal plane has 400 mm of the aperture diameter, and this consists of the multi-chroic transition-edge sensor (TES) bolometers. The TES detectors in this focal plane are cooled down to 100 mK. Due to this system, the LFT will satisfy the requirement of the sensitivity for the detection of the primordial B-mode, 2.0 μK·arcmin.

2.5   LFT polarization modulator unit

The PMU are the instrument to control major noise and systematic effects. The CAD design of the current LFT PMU model is shown as Figure 2.5. The LFT PMU will employ the multi-layer achromatic half-wave plate (HWP) made of the sapphire in order to cover the LFT frequency bandwidth (12; 50; 13).

The HWP can rotate the incident linear polarization signal $2 \times \chi$, where χ is the angle between the incident polarization angle and the optic axis of the HWP. This process is shown as Figure 2.6. Defining the rotational frequency of the HWP as f_{rot}, this makes the sky signal to up-convert at the rate of $4f_{rot}$ (15; 16), as shown in Figure 2.7. Therefore, this mechanism can reduce the effective instrumental polarization effects, called $1/f$ noise.
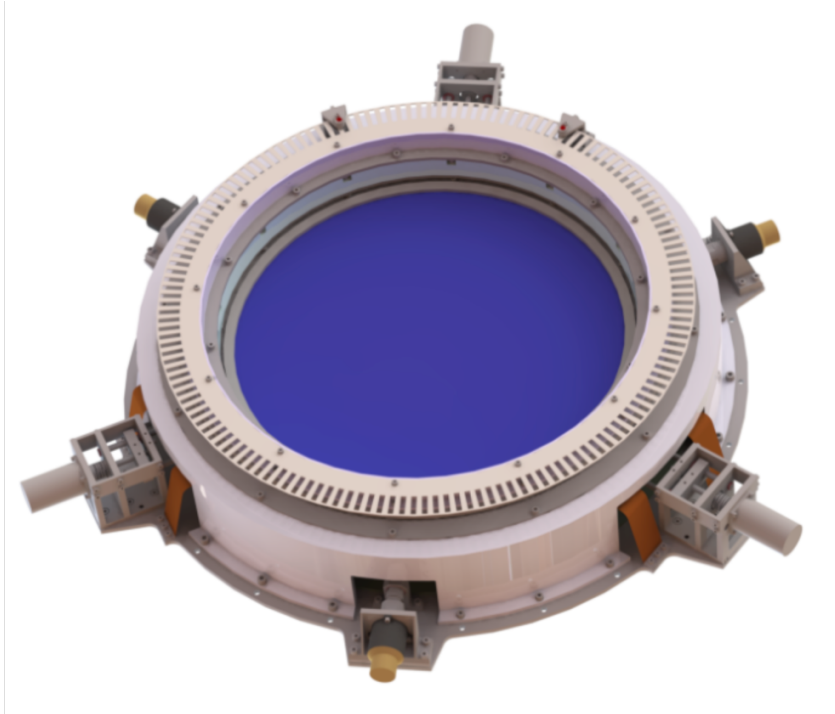
Figure2.5　The CAD model of the LFT PMU in LiteBIRD （11）. The HWP consists of five a-cut sapphire plates, and we stack them with different configuration in the optic axis for the broadband operation （12; 13）. We machine sub-wavelength structures (SWS) on the outside of plates as a broadband anti-reflection （14）.
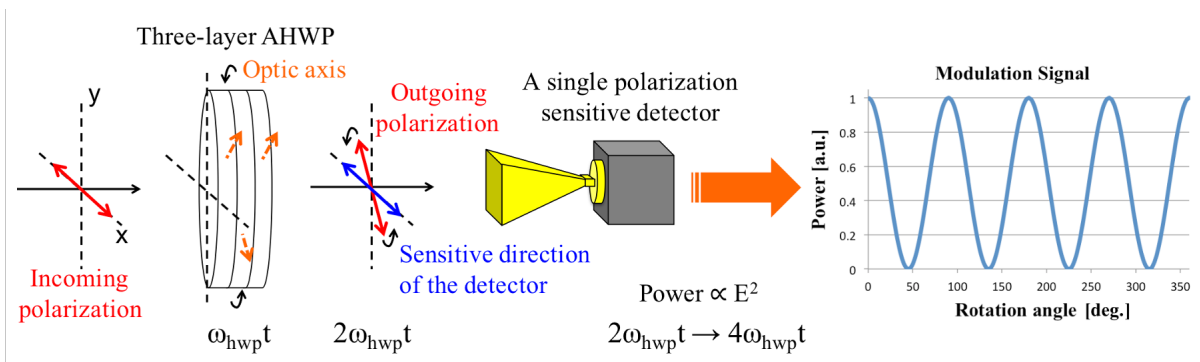
Figure2.6　The modulation mechanism of an incident polarization signal with three-layer AHWP （15）.
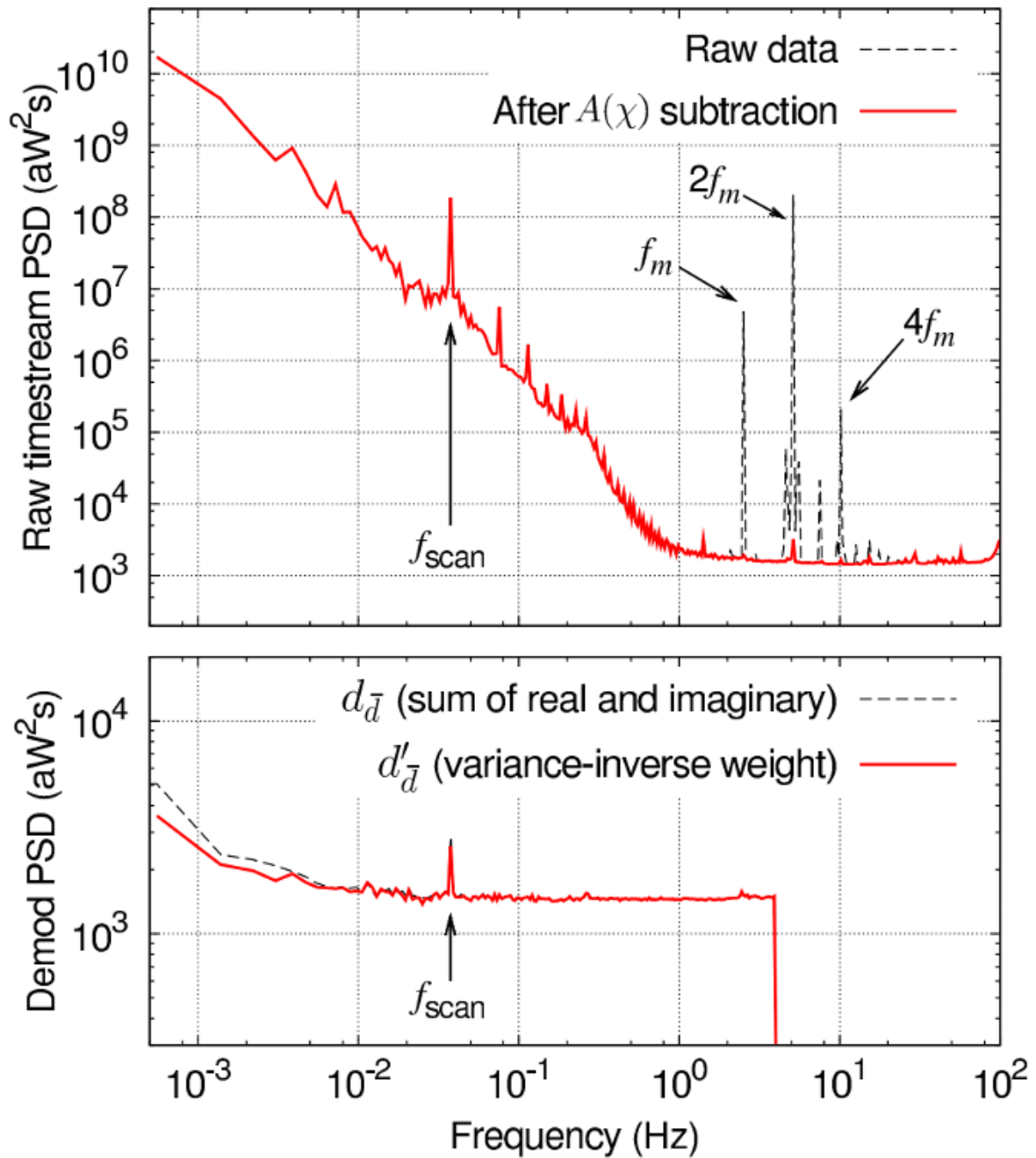
Figure2.7 The PSD of modulated signal and demodulated signal in Aatacama B-mode Search (ABS)（16）.

In general, the reconstruction of linear polarization signals requires the orthogonal detectors. In this measurement, the difference of both detector performances is the origin of systematic effects. For example, signals of orthogonal detectors can be shown as

$$d_a = g_a(I + Q\cos2\phi_a + U\sin2\phi_a), \tag{2.3}$$
$$d_b = g_b(I + Q\cos2\phi_b + U\sin2\phi_b), \tag{2.4}$$

where g_a and g_b are gains of both detectors, and ϕ_a and ϕ_b are polarization angles for both detectors. Stokes parameters are calculated by the difference of d_a and d_b, shown as

$$\Delta d = (g_a - g_b)I + (g_a\cos2\phi_a - g_b\cos2\phi_b)Q + (g_a\sin2\phi_a - g_b\sin2\phi_b)U. \tag{2.5}$$

Therefore, Δd will have the unpolarized component depending on the difference of gains of both detectors. With the HWP polarimetry, we can measure the linear polarization signal with a single polarization sensitive detector. This can reduce the systematic effect due to the difference of detectors' performances which is shown above.

The continuous rotating mechanism of the PMU will adopt a superconducting magnetic bearing (SMB) and a brush-less motor to reduce the instrumental heat dissipation. The prototype of the LFT PMU is shown as Figure 2.8. The development of this prototype is described in the following sections.

The SMB is the levitation system by using permanent magnets and high temperature superconductors (HTS). The PMU rotor which have the HWP has a ring-shaped array consisted of the segments of permanent magnets at the bottom. And the HTS also has a ring-shaped array and is fixed under the PMU rotor. In the cooled environment at less than the transition temperature of the used HTS, the SMB is activated and the magnets are fixed by a pinning effect in axial and radial directions. Because the PMU will be operated at less than 10 K in space, the SMB can be activated and the rotor can be levitated without any contact.

As the driver mechanism for the continuously stable rotation of the HWP, the PMU mounts the brush-less motor. Compared to the brushed motor, this motor realize the continuously stable rotation with lower heat dissipation, which is one of the instrumental systematic effects shown in Section 2.6. This motor consists of coils implemented in the PMU stator and permanent magnets implemented in the PMU rotor. With flowing three-phase alternating currents (AC) in coils, the PMU rotor can rotate at the rotational
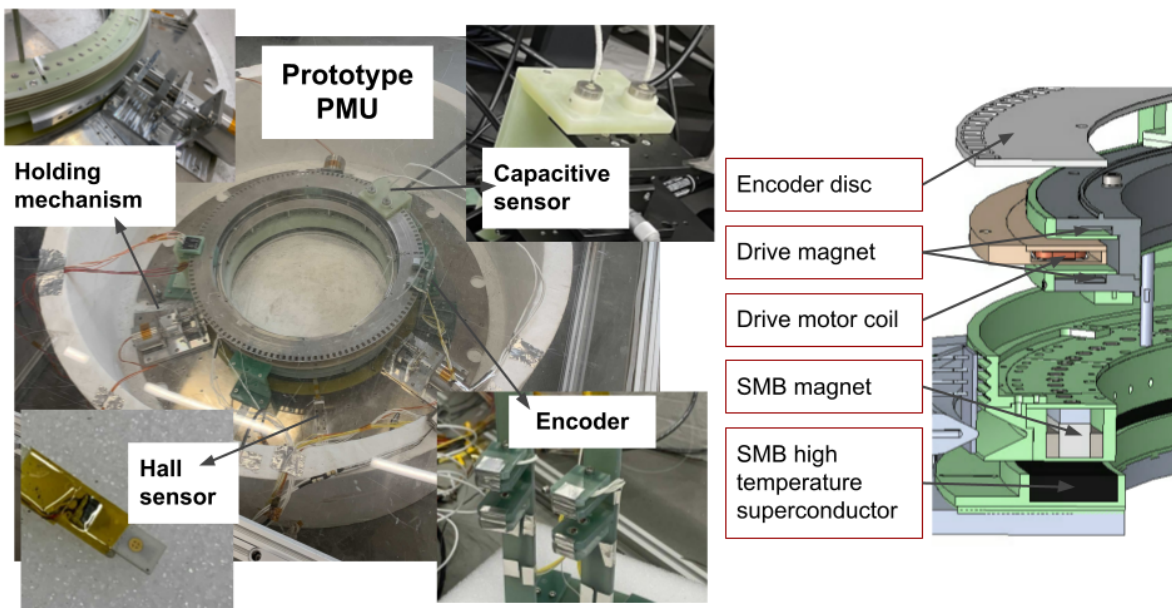
Figure2.8   Left: the overview of the prototype of LFT PMU and major instruments mounted on the PMU. Right: the cross section of LFT PMU. This figures are based on (11; 17).

frequency f_{rot} according to

$$f_{rot} = f_c/(P/2), \tag{2.6}$$

where f_c is the frequency of currents, and P is the poles of permanent magnets for driving.

Before the launch of LiteBIRD, the PMU rotor will be fixed by cryogenic grippers and the holding mechanism. In the space, grippers are released from the PMU rotor in the proper height to the HTS. The PMU rotor is expected to rotate for three years. The rotor will be held by grippers when the HWP has an unexpected temperature or emergency cases.

2.6   Purpose of this thesis

As mentioned, the LFT PMU can reduce the $1/f$ noise and systematic effects in the observation of the primordial B-mode. And the focal plane will have amounts of TES bolometers to satisfy the necessary sensitivity. On the other hand, the PMU makes its instrumental systematic effects. Table 2.9 shows the current design guidance values for the engineering model and the flight model (EM and FM) of the LFT PMU. The design of

Parameter	BBM target	Achieved	Rationale
HWP optical area	≥300 mm	330 mm	For demonstration toward the demonstration model of $\phi \sim$500 mm
HWP transmittance (34 - 161 GHz)	≥ 97%	91%~98%	Sensitivity calculation, frequency-dependent requirements should be given by a detailed systematic error study
HWP polarization efficiency (34 - 161 GHz)	≥ 98%	80%~99%	Same as above
HWP temperature	≤ 20 K	34 K	From optical loading requirement in sensitivity calculation
Heat dissipation	≤ 4 mW	~20 mW	Budget assigned from cooling power of 4 K JT cooler
Rotation frequency	46 rpm	30~120 rpm	Negligible $1/f$ noise
Encoder accuracy	0.5 arcmin	0.25 arcmin	Tentative polarization angle requirement of $\Delta\alpha \leq$1 arcmin[13]
Mass	≤20 kg	34 kg	≤30 kg for DM of $\phi \sim$500 mm, satellite system resources and cooling power

Figure2.9   Table of target values and achieved values of the prototype instruments of the LFT PMU (11).

EM/FM of the LFT PMU is polished up by the evaluation results of the prototype of the LFT PMU.

   This prototype is designed, developed, and tested in Kavli Institute for the Physics and Mathematics of the Universe (IPMU), the University of Tokyo, Japan. The prototype is the semi-real size model which has the diameter of 330 mm as the size of the AHWP. Each parameter shown in Table 2.9 is measured in the experiment of each individual instrument, not in the experiment using the integrated model of the HWP and the rotation mechanism. For example, the transmittance of the HWP is tested by using small size model, whose diameter ϕ is 50 mm, of two-layer AHWP (14; 51). This has the Sub-Wavelength Structure (SWS) on top surface and bottom surface of two-layer sapphires. The SWS has the roll of the broadband anti-reflection to satisfy the target values of the transmittance. This structure has the pyramidal shape, which are fabricated by the ultra-short pulsed laser ablation, and this structure is shown in the left panel of Figure 2.10. The transmittance depends on the frequency of light. In the experiment at room temperature, the transmittance in the target frequency range of LiteBIRD LFT has achieved from 91 % to 98 %, shown in the right panel of Figure 2.10. As another example, we have the target value in the instrumental
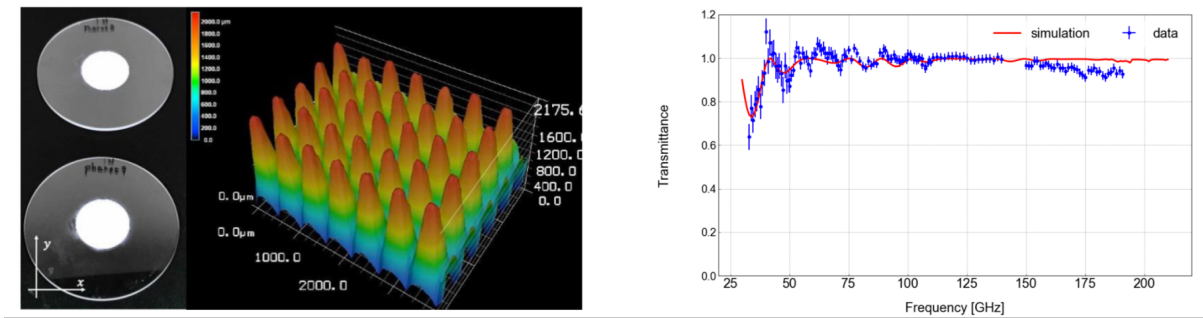
Figure2.10 Left: small size samples that the SWS was fabricated, and a confocal microscopy image of the SWS shape. Right: the transmittance performances of the small size five-layer AHWP, which has the SWS in the top and back surface (14; 11).

heat dissipation (11). The prototype of the rotation mechanism is tested in the 4K Gifford-McMahon (GM) cryostat, shown as Figure 2.11, at the laboratory experiment. This has 1.5 W cooling power at the 4 K stage, and cools down less than 10 K. The prototype of the rotation mechanism gives off the heat by i) the light emitting diode (LED) of the optical encoder, which has explained in Section 3.2, ii) the Joule heat due to the three-phase current, and iii) the eddy current and the hysteresis loss due to the SMB. Second and third components are produced when the PMU rotor spins. Especially, third component is calculated from the rotational frequency decay when the PMU rotor spins freely, and the value is estimated as ∼20 mW (11).

In this thesis, we focus on systematic effects produced by the rotation mechanism. Especially, we discuss the reconstruction accuracy of the rotational angle of HWP and the potential effects of the vibration of the PMU rotor.
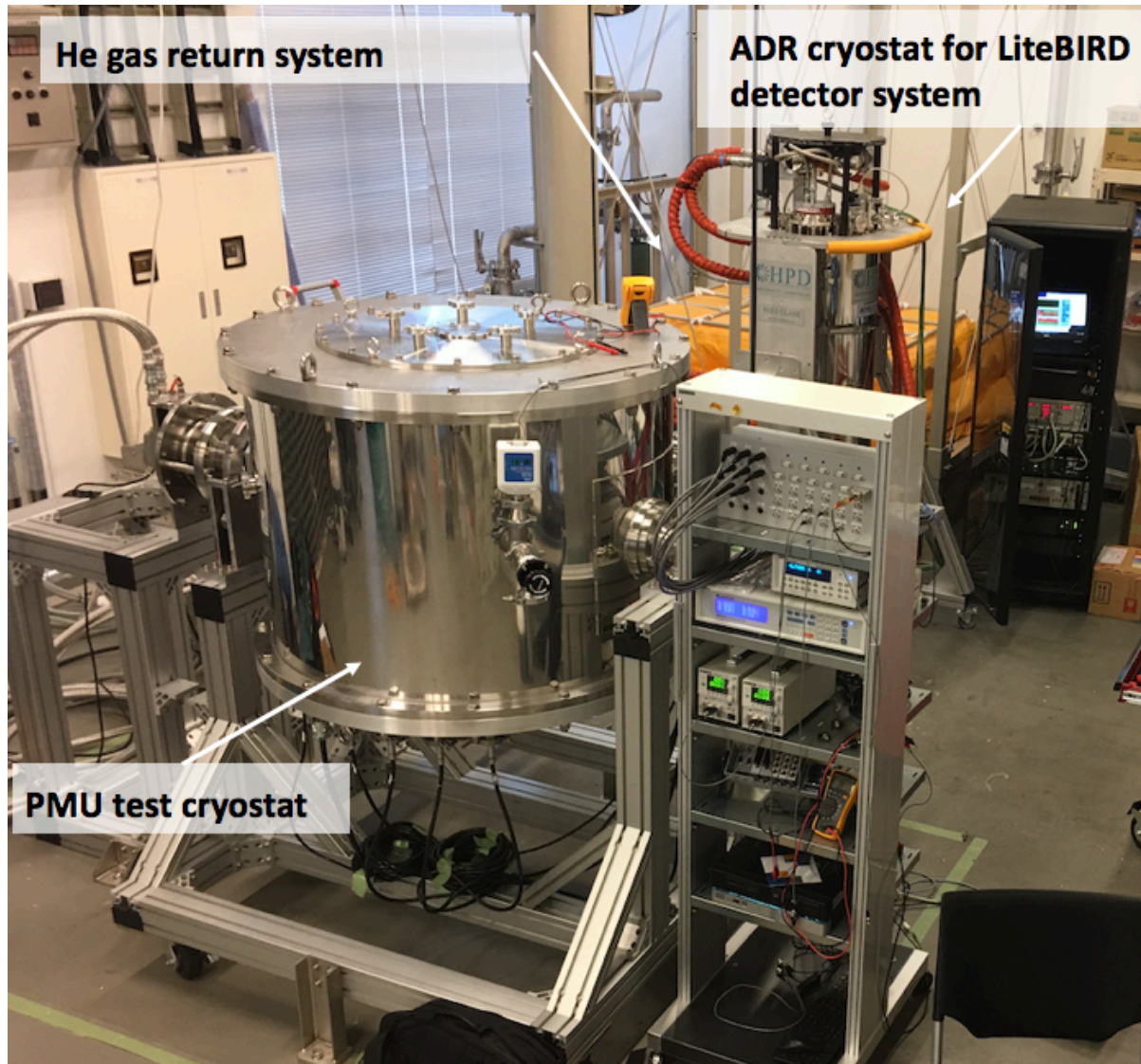
Figure2.11   The 4K GM cryostat for PMU test and the adiabatic demagnetization refrigerator (ADR) cryostat for LiteBIRD detector system in Kavli IPMU.

Chapter 3.

Reconstruction of polarization angles

3.1   Requirement

LiteBIRD observes the CMB polarization surveying all sky. The observed signal is modulated by the PMU, and the modulated signal is described as a linear combination of Stokes parameters. When we define the modulation signal as d, this is shown as

$$d = \frac{1}{2} \left(I_{in} + \epsilon Q_{in} \cos 4\rho_h + \epsilon U_{in} \sin 4\rho_h \right) \tag{3.1}$$

$$= \frac{1}{2} I_{in} \left[1 + \epsilon P_{in} \cos \left(4\rho_h - 2\alpha_{in} \right) \right], \tag{3.2}$$

where I_{in}, Q_{in} and U_{in} are the Stokes parameters of incident linear polarization signals, P_{in} is the polarization fraction ($\sqrt{Q_{in}^2 + U_{in}^2}/I_{in}$), ρ_h is the position angle of the continuous rotating HWP, and α_{in} is the polarization angle of the incident polarization. The phase of the modulation signal, ϕ, is in the relation with the polarization angle as $4\phi = 2\alpha_{in}$ (52) . Therefore, we measure the polarization angles by the position angles of the continuous rotating HWP. The method how we reconstruct the HWP position angles is shown in Section 3.2. The reconstruction accuracy of the polarization angle, defined as $\Delta\alpha$, is one of the systematic effects introducing the E-mode leakage in the observed B-mode. The observation results of WMAP (27) shows that the power spectrum of the observed B-mode, $C_\ell^{BB,obs}$, is shown as

$$C_\ell^{BB,obs} = C_\ell^{EE} \sin^2(2\Delta\alpha) + C_\ell^{BB} \cos^2(2\Delta\alpha), \tag{3.3}$$

where C_ℓ^{EE} is the power spectrum of the E-mode, and C_ℓ^{BB} is the power spectrum of the primordial B-mode. The term $C_\ell^{EE}\sin^2(2\Delta\alpha)$ is the leakage of E-mode depending on $\Delta\alpha$ in the observed B-mode.

The design guidance value of the accuracy of the polarization angle is required for the develoment and the evaluation of the prototype of the LFT PMU. Currently, the value is assigned as 1 arcmin for the accuracy of the polarization angle. Thus, the design guidance value of the accuracy of the HWP position angle is 0.5 arcmin.

This chapter is based on S. Sugiyama et al. (18). And figures are quoted from (18).

3.2   Measurement method

Rotation mechanism and optical encoder

We measure the HWP position angle by counting optical encoder signals modulated by an optical chopper, which are shown in Figure 3.1. The optical encoder consists of a light
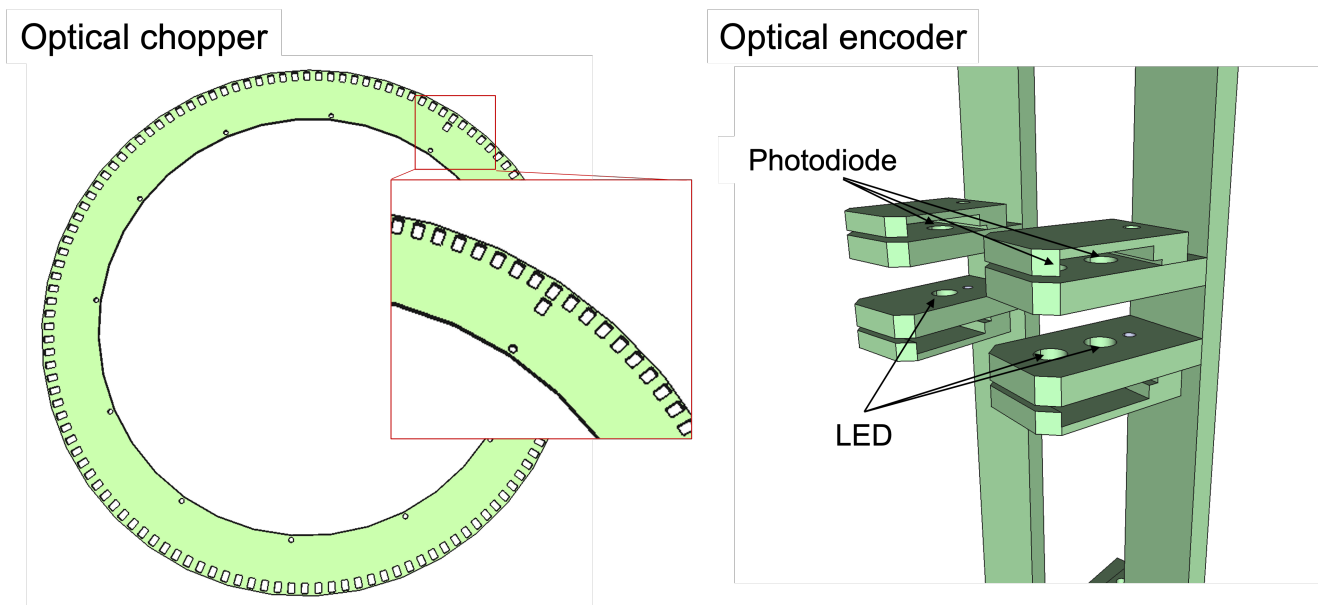
Figure3.1   The CAD models of an optical chopper and an optical encoder. Figures are based on (18).

emitting diode (LED) and a silicon photodiode (SiPD). The optical chopper mounted on the prototype of the LFT PMU has 128 slots, which has the rectangular shape, on the outer circumference of the chopper. The encoder reads vacant slots of the rotated encoder

disc. When the encoder disc rotates periodically, the shape of the signal of the SiPD is expected to be periodic square waves. Figure 3.2 shows sample signals obtained by encoders, described on Section 3.3. In this figure, we see signals of two encoders set at the positions of 128 slots, called A and B phases, and one encoder set at the position of 1 slot, called Z phase.
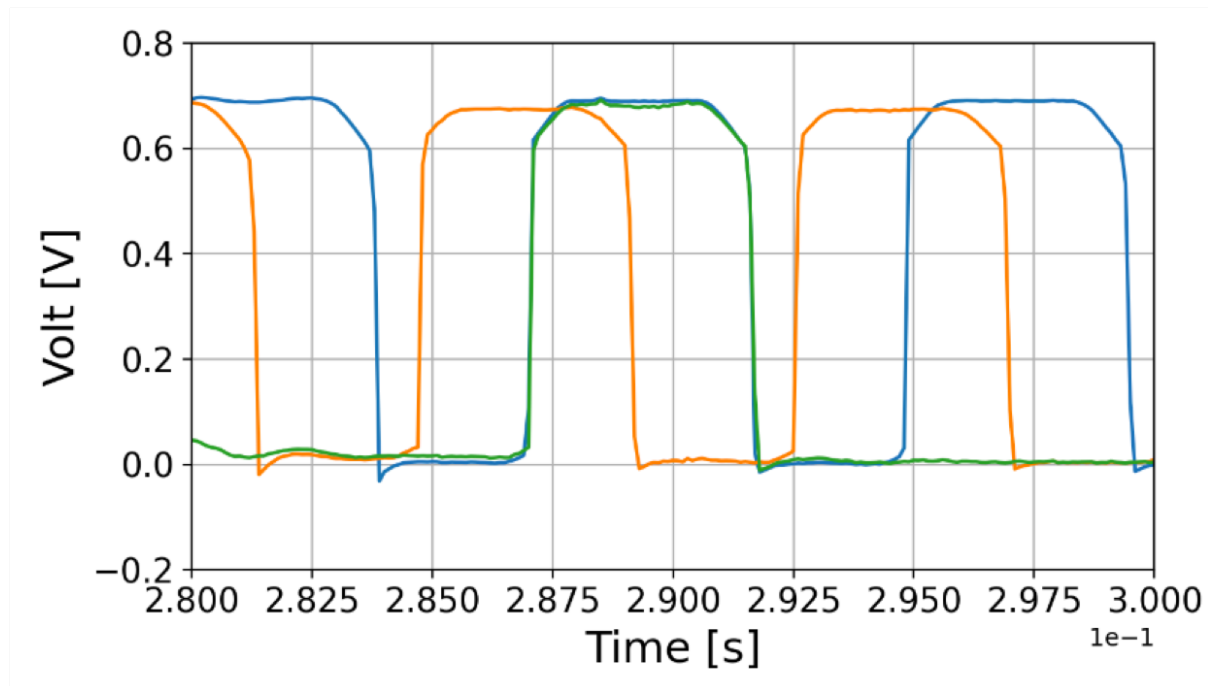
Figure3.2   The signals of encoders at 1 Hz rotation. Blue and orange curves are the output of encoders set at the position of 128 slots, and green curve is the one at the position of 1 slot. This figure is based on the study (18).

Bandwidth constraints

The encoder signal data of HWP position angles shall be reduced because of the limited transmission bandwidth between the Sun-Earth second Lagrange point and ground stations. For a deep space mission, the typical telemetry is to use X-band (10 Mbps). In recent years, a broader bandwidth, Ka-band (128 Mbps or more), is available, but it depends on a weather conditions on Earth.

The allocated data rate for the encoder signal will be a small fraction of the available total bandwidth because a large fraction of the transfer data volume is taken by the detector signals. Assuming we can assign 1 hour for the data transfer time in one day, the total

transferable data is 45 GB and 576 GB for X-band and Ka-band, respectively. An assumed 0.1 % of the total data volume can be allocated for the HWP encoder data, the target value of the transferable data volume is 0.62 GB per day.

Based on the target value of the angle reconstruction accuracy of 0.5 arcmin, a required sampling rate of one encoder signal becomes 43.2 kHz at 1 Hz rotation. Assuming the sample data resolution as 2 Bytes, the corresponding bandwidth is 86.4 f_{rot} kBps per encoder. Therefore, the data transfer volume per day is equivalent to 7.46 GB per encoder. This far exceeds the estimated data volume for the encoder signal data. Therefore, we need on the board algorithm to reduce the encoder signal data.

Algorithm for the position angle reconstruction

The left panel of Figure 3.3 shows the block diagram of the developed algorithm to calculate the periods of encoder signals. We set thresholds at 3/4 and 1/4 of the maximum
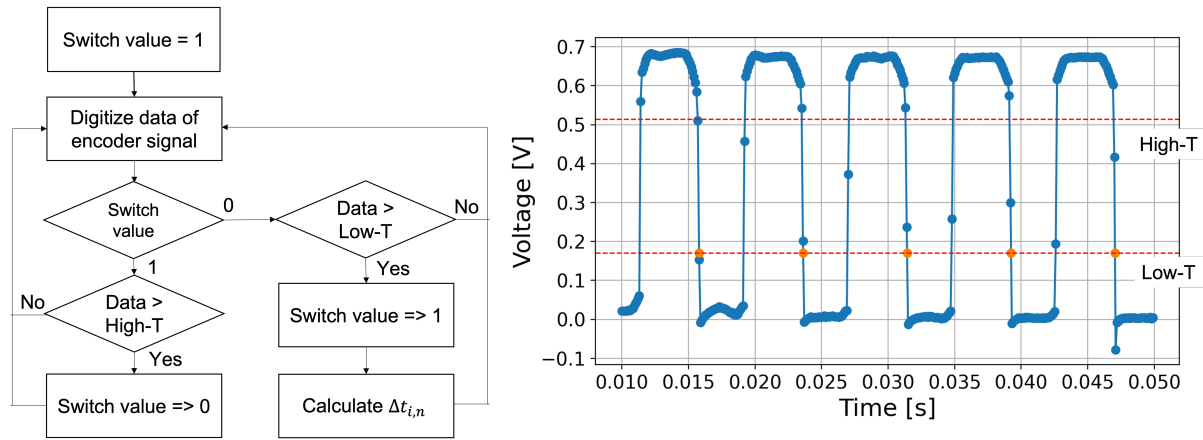
Figure3.3   Left: block diagram of the developed algorithm. Right: outputs of the encoder (blue curve) and the developed algorithm. Red dash lines are thresholds at 3/4 and 1/4 of the maximum voltage. Orange data are the points of intersection of an encoder signal and the lower threshold. Figures are based on (18).

voltage of encoder signals (see the right plot of Figure 3.3) to detect the edge of each pulses. This is an applied Schmitt trigger method, which is robust against noise in the encoder signal (53) . Extracting two successive data points above and below the lower threshold, we calculate the time of the intersection point between the lower threshold and the linearly interpolated line from two data. The time of the intersection point is defined as $t_{i,n}$. The

subscripts of i and n are the slot position number and n^{th} rotation, respectively. By using $t_{i,n}$, the periods of encoder signals in A and B phases can be defined as $\Delta t_{i,n}$ and shown as

$$\Delta t_{i,n} = t_{i+1,n} - t_{i,n}. \tag{3.4}$$

The same derivation is used for the period of Z phase, Δt_n^Z. This period is corresponding to the rotation period. The rotation angle per each slot $\rho_{i,n}$ is shown as

$$\rho_{i,n} = 360 \, \bar{f_{rot}} \, \Delta t_{i,n} degree, \tag{3.5}$$

where $\bar{f_{rot}}$ is the rotational frequency of the encoder disc. Assuming f_{rot} is constant, the error of rotational angles per slot can be defined as

$$\sigma_\rho = 360 \, \bar{f_{rot}} \, \sigma_{\Delta t} degree, \tag{3.6}$$

where $\sigma_{\Delta t}$ is a standard deviation of measured periods in A and B phases, and this is shown as

$$\sigma_{\Delta t} = \sqrt{\frac{1}{N-1} \sum_{i=1}^{128} \sum_{n=1}^{n<n_T} (\Delta t_{i,n} - \frac{1}{N} \sum_{i=1}^{128} \sum_{n=1}^{n<n_T} \Delta t_{i,n})^2}, \tag{3.7}$$

where N is the number of periods at B phase, T is the acquired time of encoder data, and n_T is the number of revolution within a period of T.

3.3   Rotation experiment

We evaluate the method described in the previous section utilizing a prototype model. The prototype of the LFT PMU, as shown in Figure 2.8, is operated on the temperature of 77 K by using liquid nitrogen (LN2) or below 10 K using the 4 K GM cryostat in Kavli IPMU. We spin the PMU rotor by using AC driver motor and measure periods of encoders at B and Z phases by the FPGA board. The raw encoder signal is processed in a 12-bit analog-to-digital converter, Pmod AD1, and a ready-made FPGA board, Spartan-6 SP605 (see Figure 3.4). The input clock frequency is 1.9 MHz, and the AD conversion needs the number of bits per sample, 19-bit. Thus, the sampling rate in the FPGA board is 100 kHz. We employ data sizes of periods of the encoder signal in B and Z phases as 3 Bytes and
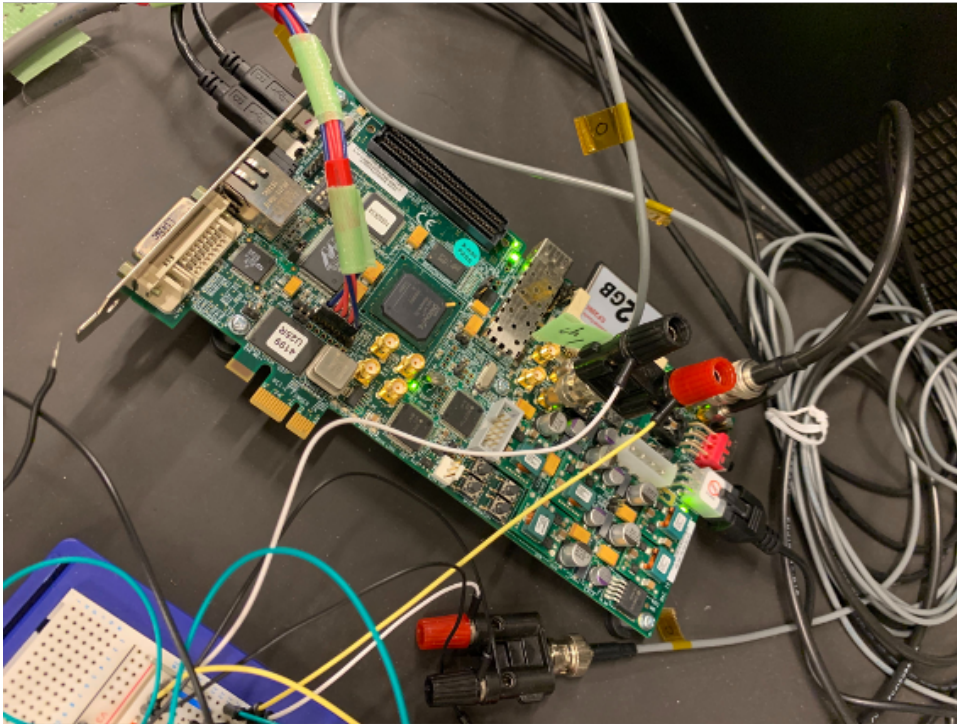
Figure3.4   The evaluation board of the FPGA used in this experiment.

4 Bytes, respectively. The data from the FPGA board are sent to the PC through a serial transmission.

We carry out the experiments under two conditions; constant rotation at 1 Hz, which is a representative rotational frequency, in 4K GM cryostat, and free rotation without any external drive torque in LN2. These results are used to calculate the total angular error and the subdivision of the error.

3.4   Result

Figure 3.5 is the recorded period from the optical encoder in B phase when we rotated the PMU rotor at 1 Hz in the 4K GM cryostat. The obtained mean of the period becomes 7.81×10^{-3} sec which is consistent with the expected value, 1/128. The derived standard deviation of periods becomes 1.15×10^{-5} sec. In the same way, the rotational frequency is calculated from the signal of the optical encoder in Z phase. The mean of the rotation frequency becomes 1.00 Hz, which is equivalent to the expected value, for 10 min. Due to Equation 3.6, the angular accuracy becomes 2.48×10^{-1} arcmin. Therefore, the value of
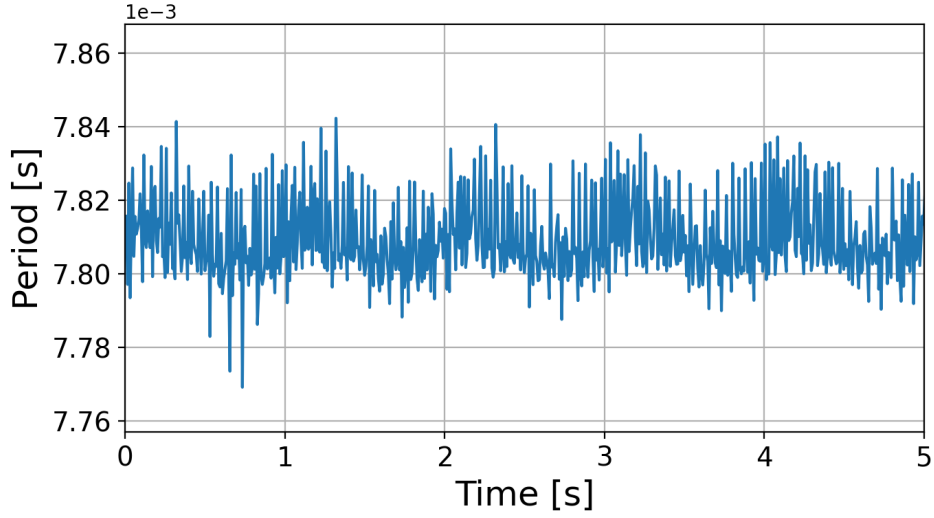
Figure3.5   The timeline of recorded periods of the encoder signal in B phase when we rotate the PMU rotor at 1 Hz in the 4K GM cryostat. The time in x-axis is the cumulative of periods. This figure is based on (18).
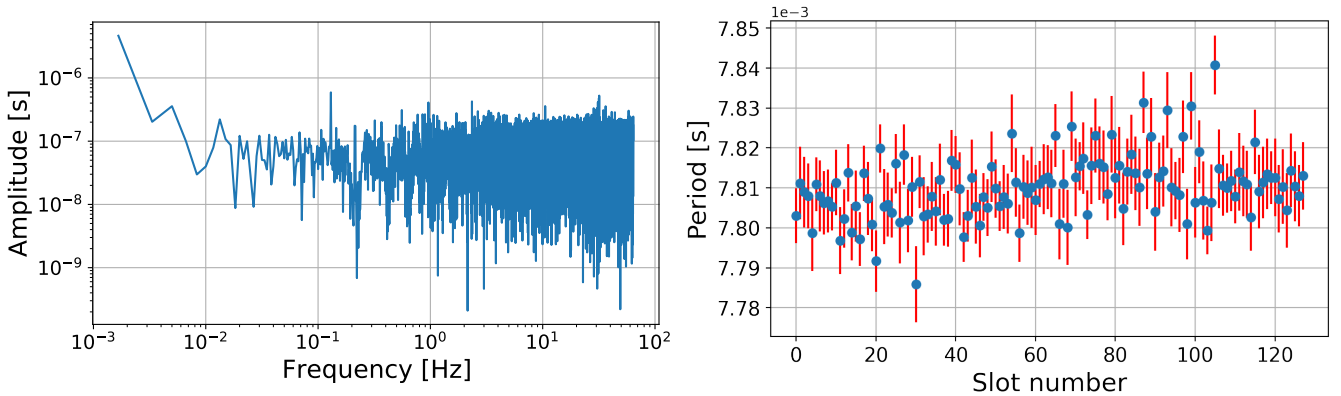
Figure3.6   Left: the nonequispaced fast Fourier transform result of the measured period, $\Delta t_{i,n}$ shown in Figure 3.5. Right: the mean and the error of the period folded within one revolution with the binning of 128 slots. The error is represented as a standard deviation of the period. Figures are based on the study (18).

measured angular error satisfies the target guidance value, 0.5 arcmin.

The left panel of Figure 3.6 shows the nonequispaced fast Fourier transform result of the measured period fluctuation. The result shows flat amplitudes above 10^{-2} Hz, and larger fluctuations below 10^{-2} Hz, and a peak at 1.30×10^{-1} Hz. The former shows the rotational stability of the PMU rotor over 10 min. The rotation stability for operating time of LiteBIRD will be required in the future experiment, more discussed in Section 5.
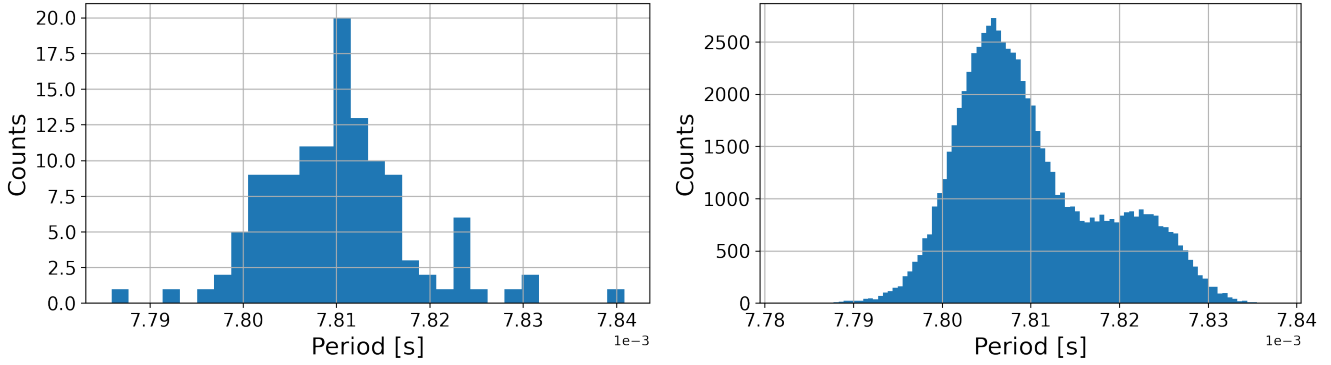
Figure3.7   Left: The histogram of the mean period in each slot position shown in the right panel of Figure 3.6. Right: The histogram of the asynchronous component of periods over 10 min. Figures are based on (18).

The right panel of Figure 3.6 shows the mean and the standard deviation of periods which are folded within one revolution by the binning of the 128 slots. There is a trend of the rotational synchronous variation within one rotation period. The left panel of Figure 3.7 shows the histogram of the mean period, as shown in the right panel of Figure 3.6. The standard deviation of this mean period is 7.88×10^{-6} sec. Therefore, the corresponding component of the angular reconstruction accuracy is 1.70×10^{-1} arcmin.

The mean of periods within one revolution can be treated as a template. We subtract this template from the whole period data to estimate the asynchronous component of the period variations over 10 min. The right panel of Figure 3.7 shows the histogram of the asynchronous component. The standard deviation of the asynchronous component of the one-slot periods over 10 min is 8.34×10^{-6} sec, therefore, this corresponds to 1.80×10^{-1} arcmin.

In the case of the continuous rotation at 1 Hz, the corresponding data volume for the periods to achieve this reconstruction accuracy is

$$(3\,\text{byte} \times 128 + 4\,\text{byte}) \times \frac{86400\,\text{s}}{1.0\,\text{s}} = 0.03\,\text{GB/day}. \tag{3.8}$$

Therefore, the transfer data volume is 0.03 GB/day when the data capacity as 3 byte and 4 byte for each period of B phase and Z phase, respectively. Assuming we require two encoders in A phase and two in B phase for higher angular resolution, the transfer data volume is 0.12 GB/day. This value satisfies the requirement of the transfer data volume, 0.62 GB/day.

Note that the total angle error shown this section is estimated from the raw periods of the encoder without any processes, such as the down-sampling process and the clock timing adjustment with LiteBIRD detectors. And it should be emphasized that the parameters used in this thesis, such as the number of slots in the optical chopper, the number of encoders, and the assigned data capacity of the period in each phase, are tentative design values.

3.5 Discussion

The measured period variations are subdivided to potential causes. As the large classification, we can split the period variations into two categories; the rotational synchronous period variation and the rotational asynchronous period variation. In this section, we discuss six potential causes in each variation, estimate their magnitudes, and compare the total accuracy shown in the previous section and the RMS of all estimations. The measured variations, estimated as potential source effects, are summarized in Table 3.1.

Non-uniformity of slot width

As mentioned, the prototype of the LFT PMU employs the aluminum optical chopper. Because the equally-spaced slots are fabricated in this chopper with medium tolerance ~0.1 mm, we expect the period variation has the error due to the fabrication accuracy.

We uses the measurement results of a coordinate measuring machine (CMM) for the estimation of the effects of the fabrication accuracy. The CMM measures the coordinates of inside of each slot, and we calculate the each width between the edges of adjacent slots. The calculated widths are shown in Figure 3.8. With this measurement result, we obtain the standard deviation of the width δ_l as 4.18×10^{-3} mm. Assuming the rotational frequency $\bar{f}_{rot}$ and the radius of the center of slots r are constant, the period variation by the width variation $\sigma_{\Delta t_{i,l}}$ is shown as

$$\sigma_{\Delta t_{i,l}} = \frac{\delta_l}{2\pi r \bar{f}_{rot}}, \tag{3.9}$$

where $\bar{f}_{rot}$ is 1 Hz and r is 243.5 mm. Therefore, $\sigma_{\Delta t_{i,l}}$ becomes 2.73×10^{-6} sec. Thus, the contribution of this cause in the angular error is estimated as 5.90×10^{-2} arcmin.
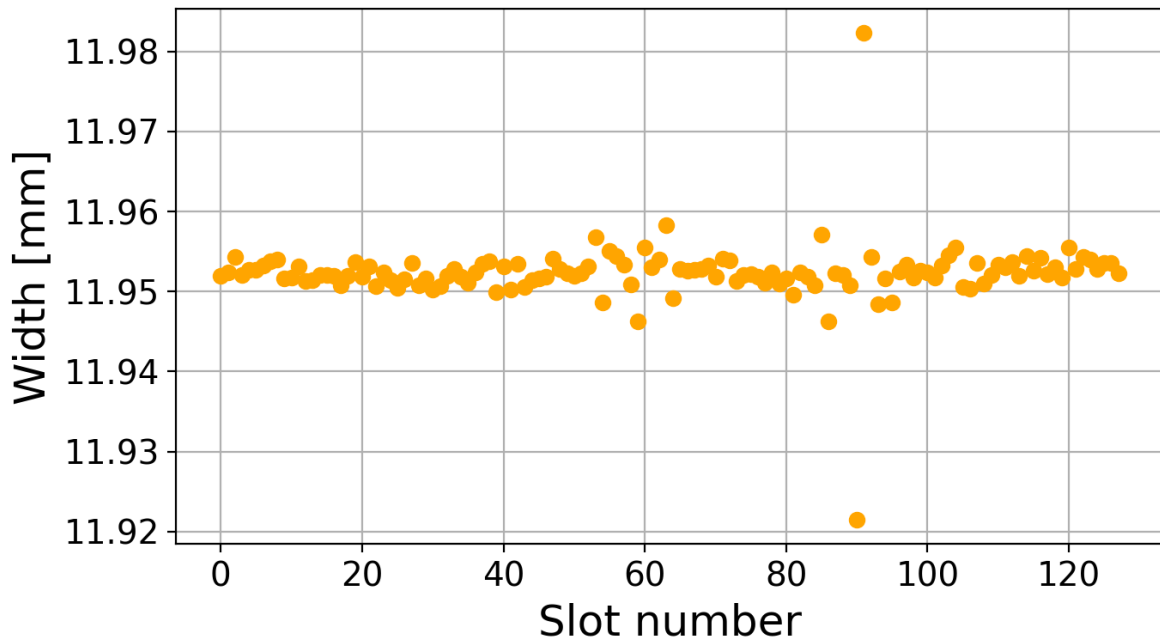
Figure3.8   The distance of adjacent slots in the optical chopper. This figure is based on (18).

Misalignment of the PMU rotor

The prototype of the LFT PMU consists of two major components; the PMU rotor and the PMU stator. Because the PMU rotor is completely non-contact, the PMU rotor is aligned only by the centering jigs to fix the rotation axis. With any misalignment in the radial direction, the encoder cannot readout the center positions of slots. This potentially causes variation in the measured period. Assuming the amplitude of the radial transitional displacement δr by 0.4 mm, which is the tolerance of the fabrication accuracy of the rotor centering jigs, the variation due to this contribution $\sigma_{\Delta t_{i,r}}$ is shown as

$$\sigma_{\Delta t_{i,r}} = \frac{l}{2\pi r^2 \bar{f}_{rot}} \delta r, \qquad (3.10)$$

where the width of slots l is 11.95 mm. In results, $\sigma_{\Delta t_{i,r}}$ can become 1.28×10^{-5} sec. Thus, the corresponding angle error is estimated as 2.77×10^{-1} arcmin.
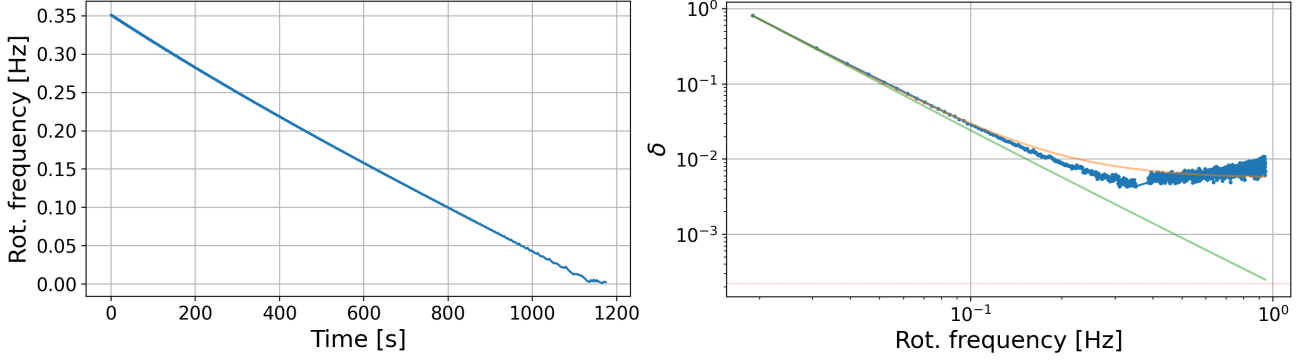
Figure3.9   Left: The rotational frequency as a function of time when the rotor freely spins down. Right: The fractional rotational frequency variation as a function of the rotational frequency obtained from the left panel. The orange is the best fit curve using a model equation in Equation 3.13. The green and pink are the first two terms and the last term of Equation 3.13, respectively. Figures are based on (18).

Magnetic field variation

The ring of the HTS and the permanent magnets are consisted of each material's cuboid segment. When the HTS ring of the SMB is cooled below its transition temperature, the HTS traps the magnetic field of rotor magnets. The traps will be happened in the same positions and this causes the torque variation during its rotation. Therefore, it makes the rotation synchronous frequency variation (54).

To distinguish the rotational period variation caused by the trapping of the magnetic field and the non-uniform torque applied by the AC motor, we estimate this contribution by the result of the free rotation experiment using LN2 bath. The left panel of Figure 3.9 shows the rotation frequency calculated by the period in B phase when the PMU rotor is in free spin. Then, the HTS ring is submerged in LN2 and the rotor is above the liquid surface. We fit the rotation frequency curve with a model as

$$f_{rot} = \frac{c}{2\pi b} \, e^{bt-a},\tag{3.11}$$

where a, b, and c are the fitting parameters. Based on the previous study, we compute the fractional speed variation in each rotation as

$$\delta = (f_{rot,max} - f_{rot,min})/f_{rot},\tag{3.12}$$

where $f_{rot,max}$ and $f_{rot,min}$ are the maximum and the minimum rotation frequencies in each rotation. The right panel of Figure 3.9 shows δ as a function of time. The model of this fitting is

$$\delta = \sqrt{1.0 + a/(f_{rot} + b)^2} - 1.0 + c. \tag{3.13}$$

The first two terms are for the fractional speed variation originated from the interference of the magnetic field, and the third term is the offset which will be due to the noise in the encoder signal. When we extrapolate the fitting model at 1 Hz, the fractional speed variation is $\delta = 2.22 \times 10^{-4}$. Then, the corresponding variation of the period is 8.80×10^{-7} sec. Therefore, this contribution to the HWP angle error is 1.86×10^{-2} arcmin.

Variation of motor drive current

The rotation of the PMU rotor is controlled by the motor drive electronics, which gives three-phase currents described in Section 2.5. If the current contains instability, the drive torque varies correspondingly. Because the drive frequency has the relation shown as Equation 2.6 and the number of poles of this motor is 24, we assign the current frequency as 12 Hz for 1 Hz of rotation.

We can propagate the angular velocity variation as

$$d\omega_m = \frac{dt\delta\tau}{I} \tag{3.14}$$

$$= \frac{dtC_\tau i_{rms}}{I} \tag{3.15}$$

where $\delta\tau$ is the torque variation, I is the inertia of the rotor, and C_τ is the torque constant. The drive current should be produced by the design to provide a fixed torque. Assuming that a feature in the current will fully contribute as the torque variation, the instability of the current variation is represented as the RMS of the motor drive current i_{rms}. The input values for the prototype system as $I = 0.67 \text{ kg m}^2$, $C_\tau = 0.59$ Nm/A, and $i_{rms} = 1.34 \times 10^{-2}$ A give

$$d\omega_m = 1.14 \times 10^{-2} \, dt. \tag{3.16}$$

Because the three-phase current is operated with the period as 1/12 sec, we introduce this value in the time scale of dt. As a result, this contribution of the period variation in the
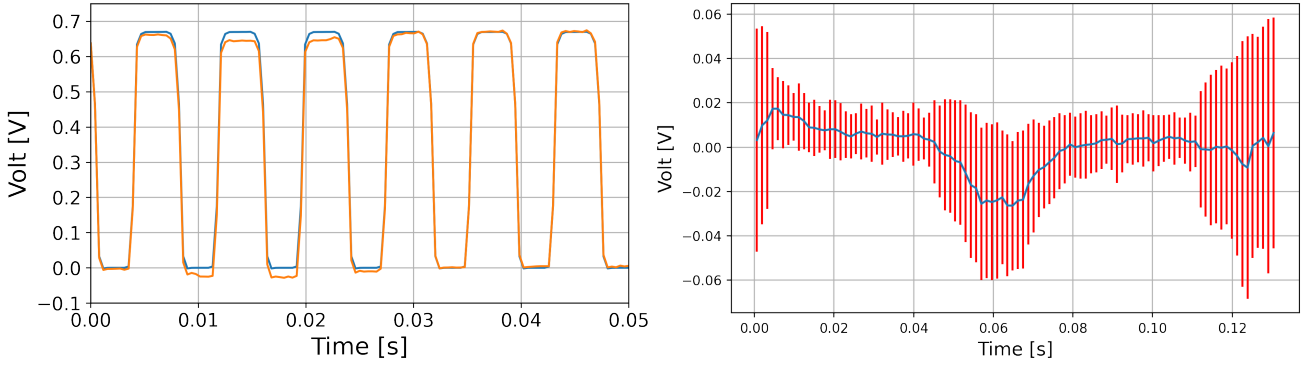
Figure3.10   Left: The simulated encoder signal with and without the estimated inter-
ference noise. Right: The template of the interference noise which has a periodicity of
$1/7.62$ sec (blue). Red bars are the standard deviation in each bin. Figures are based on
(18).

time scale of each slot becomes 1.18×10^{-6} sec. The corresponding angular error is
2.55×10^{-2} arcmin.

Interference noise in encoder data

The noise in the encoder signal can contribute as the rotational asynchronous period
variation. Two components is expected as the components of noise: the white noise and
the periodic noise at the frequency of 7.62 Hz and its harmonics. The latter is produced by
the interference of the motor drive electronics. The used interfaces are also the prototype,
therefore, it can be improved in the future design iteration. The left panel of Figure 3.10
shows the template continuous signal of the encoder signal in B phase. The difference
between the two curves, shown as blue and orange, is the interference noise. The shown
signal without this noise is created by a template of one pulse, which is the averaged pulse
of the real encoder signal. Then, we subtract this template from the real encoder data and
fold the residuals to the periodicity at 7.62 Hz. The right panel of Figure 3.10 shows the
mean and standard deviation of the binned interference noise. We analyze the simulated
signal merged the continuous template signal and the binned interference noise by using
a python based software which has the same algorithm implemented on the FPGA board.
The period variation from this interference is 7.25×10^{-6} sec, and the corresponding
angular error is 1.57×10^{-1} arcmin at 1 Hz of the rotational frequency.

We also estimate the impact from the white noise, which is represented as the recorded voltages when we turn the driver off. Then, the standard deviation of the voltage is 4.40×10^{-4} V. This white noise contributes to the period variation to be 3.60×10^{-7} sec. The corresponding angular error is 10^{-2} arcmin at 1 Hz rotation.

Summary of the estimations

The estimated period variations and angular error are summarized in Table 3.1. The total period variation is 1.15×10^{-5} sec, and this corresponds to the reconstructed angle variation of 2.48×10^{-1} arcmin at 1 Hz of the rotation frequency. This satisfies the established design guidance value, 0.5 arcmin, in this paper. Note that this angle variation is based on the assumption that the rotational frequency of the rotor is constant over 10 min and the absolute time of period acquisitions are tagged by other system.

Among all the potential sources that cause the period variation, we can identify the rotor misalignment and the interference noise in the encoder signal from the motor driver are large contributors. The misalignment effect is expected to be shown as the sine wave of the rotational frequency in periods. Thus, the trend can be reduced by the period calibration. The interference effect is not intended and this is found during the prototype demonstration. We expect to suppress this contribution and the total contribution is expected to decrease according to the improvement of the PMU design. The next leading contributor is the non-uniformity of the slot width. While this is due to the fabrication accuracy, we do not expect that this slot width variation changes over time. Therefore, we expect to construct the angle template of from the width results and calibrate this effect.

Finally, we compute the total HWP angle accuracy using all estimated contributions of potential sources as root mean square. This value is comparable to the measured total angle accuracy, and we expect the difference of both values is due to the upper limit of the prototype of the PMU rotor misalignment.

Table3.1   The variations of the period and reconstructed angle. They are listed in the order of the total, the rotational synchronous component, the asynchronous component, and all expected contributions. This table is based on the study (18).

Sources	Period variation [s]	Angular error at 1 Hz rotation [arcmin]
Measured total variation	1.15×10^{-5}	2.48×10^{-1}
Rot. synch. comp.	7.88×10^{-6}	1.70×10^{-1}
Asynch. comp.	8.34×10^{-6}	1.80×10^{-1}
Algorithm	$< 10^{-15}$	$< 10^{-11}$
Uniformity of slot width	2.73×10^{-6}	5.90×10^{-2}
Rotor misalignment	1.28×10^{-5}	2.77×10^{-1}
Magnetic field variation	8.80×10^{-7}	1.86×10^{-2}
AC motor contribution	1.18×10^{-6}	2.55×10^{-2}
Noise in the encoder signal	7.25×10^{-6}	1.57×10^{-1}
RMS	1.50×10^{-5}	3.25×10^{-1}

Effects of a total angular error in the power spectrum

The total angular error is estimated from the result of the rotation experiment for 10 min, at 1 Hz. In this section, we estimate how the angular error will give the effects in the primordial B-mode observation.

Figure 3.11 shows expected power spectra of the primordial B-mode depending on each value of r, B-mode happened by the gravitational lens effect, and E-mode leakage given by the estimated angular error components. All spectra are from the results of pure CMB by the observation of $Planck$ (6) and using CAMB (55; 56) and healpy. The power spectrum of the primordial B-mode, shown as the top blue curve, is based on the r value expected from Starobinsky model, 0.004 (57; 8). The E-mode leakages are shown as solid line curves, whose powers are below $\sim 10^{-7}$.

We aims to detect the power spectrum of the primordial B-mode higher than the one of
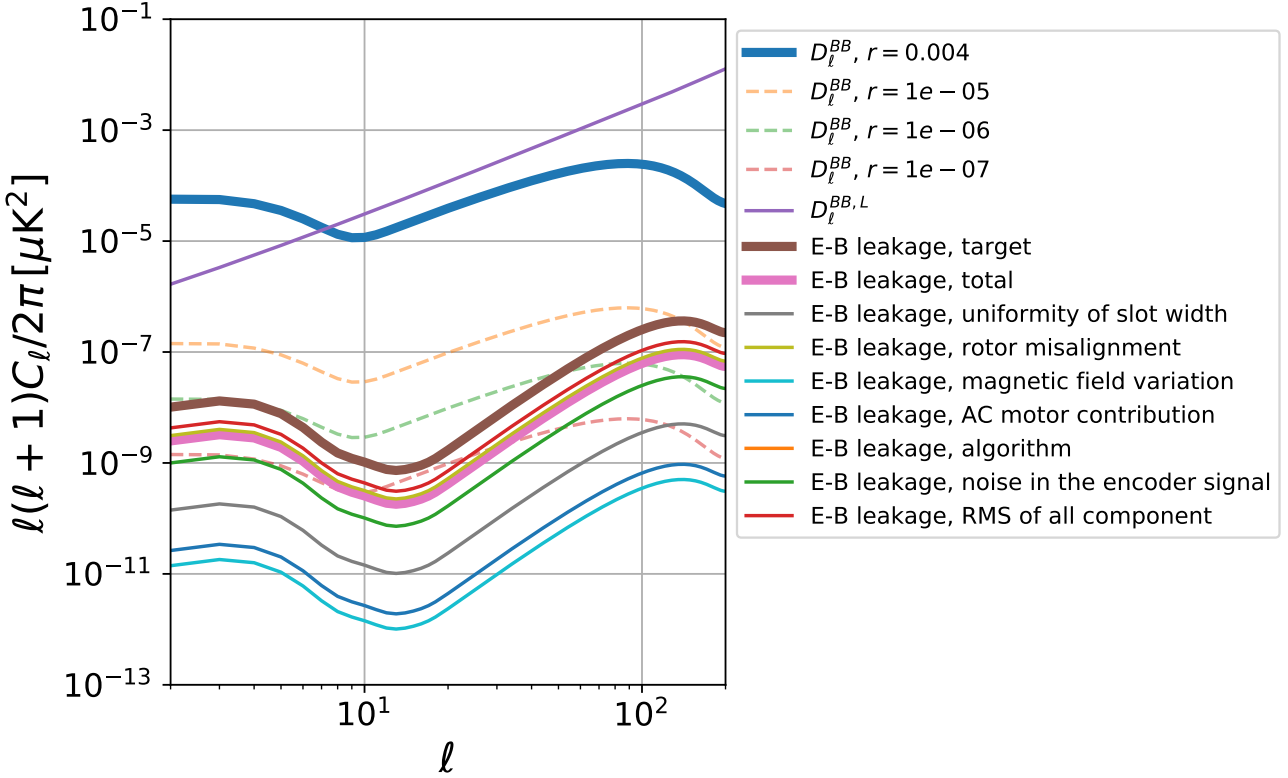
Figure3.11   The power spectra of the primordial B-mode with each r value, B-mode due to the gravitational lens effect, and E-mode leakage with the estimated angular error components.

B-mode due to the gravitational lens effect shown as the pink curve. Especially, there is the noticeable bump around $\ell \sim 2$. This is called reionization bump, which is explained in Section 2.1 and targeted by LiteBIRD. We focus on the multipole range of the bump $2 < \ell < 10$. Against the total power spectrum of E-mode leakage estimated by this study, we can compare the power spectra of the primordial B-mode with each tensor-to-scalar ratio r. The comparison shows the E-mode leakage is below the order of the primordial B-mode power spectrum with $r = 10^{-6}$ in the focused multipole range. In terms of power, the leakage is roughly four magnitude below of the primordial B-mode power at $r = 0.004$.

Chapter 4.

Extra effects due to the PMU rotor vibration

4.1 Requirement

The PMUs of LiteBIRD employ the supermagnetic conducting bearing (SMB) system, which is a completely contact-less cryogenic rotation mechanism. The SMB consists of the permanent magnets and the high temperature superconductors (HTS). The PMU rotor consists of a ring-shaped permanent magnet, and the stator consists of the HTS. Under the critical temperature of the HTS, the permanent magnet is pinned in axial and radial directions by flux pinning. There is not the physical friction between the rotor and the stator. The PMU rotor is expected to have the vibrations vertically and horizontally in resting state (58) and during the rotation. LiteBIRD LFT will accommodate a total of $\geq$ 4000 transition edge sensors (TES) in the focal plane. Even a tiny fluctuation of an external magnetic field at the focal plane may generate an extra effects in detectors, therefore, we must care the environment around the focal plane. On the other hand, the LFT PMU will be mounted near the focal plane (See Figure 2.4). The LFT PMU has the contact-less bearing and strong magnets, and the prior paper have reported the rotor has the vibration. Potential effects of this vibration has the possibility to become one of the critical origin of the primordial B-mode observation.

We investigate properties of the vibration of the PMU rotor, such as the external magnetic field due to the SMB, when the rotor is at states of a continuous rotation and resting. In

this chapter, we describe the experimental investigation of the vibration amplitude using the PMU prototype for LiteBIRD LFT. The works reported here are parts of developments and evaluations of this prototype, and all are contributed to the designing of EM/FM of LFT PMU.

This chapter is based on S. Sugiyama et al. (17). And figures are quoted from (17).

4.2   Measurement method

To investigate the effects of the PMU rotor vibration experimentally, we use the prototype of the LFT PMU, as shown in Section 3.2, with the capacitive sensor[1] and the Hall sensor[2], as shown in Figure 2.8.

The prototype of LFT PMU is scaled to about 0.7:1 with respect to a design of the flight model. As shown above, this prototype consists of the ring-shape permanent magnet. This ring-shape magnets is the array of segmented magnets that is radially magnetized. The inner radius of the magnet is 203 mm, the outer radius is 215 mm, and the thickness is 14 mm. The prototype stator consists of segmented YBCO high temperature superconductor array. There are 18 arc-shape bulk YBCO tiles, and the diameter becomes 400 mm. The rotation of the prototype rotor is driven by a contact-less AC motor. For this mechanism, there is the other ring-shaped magnet in the rotor and an array of coils in the stator (See the right panel of Figure 2.8). The rotation is controlled by three alternating currents that are shifted phases of 120 degrees. The rotation speed of the rotor is monitored by two optical encoders with a 128-slots encoder disc at the top of the PMU rotor.

We use a capacitive sensor to measure the distance between the bottom surface of the sensor and the top surface of the encoder disc. The capacitive sensor is a non-contact sensor, which generates the voltage V_c depending on the distance between the sensor and the object, d_c. We calibrated voltages by measuring distances between the sensor and Z stage with the height gauge at room temperature. The used instruments are shown in Figure 4.1. The Z stage is moved in steps of $\sim$1 mm. The measurement of the outputs is carried out in each elevation and the sampling rate is 10 kHz. We conduct each test for 10 times. Figure 4.2 and Figure 4.3 show the results when we move up and down the Z stage,

---

[1] Capacitec, model number: HPC-375E
[2] Lakeshore, model number: BHT-921

respectively. There is the linear relation from the distance range from 0 mm to 6 mm. When we assign the mean of fitting results in the experiment which we move down the Z stage as the inclination and the interception of the linear relation, the linear relation can be shown as

$$V_c = 1.68\,d_c + 0.51. \tag{4.1}$$

We also measure the magnetic field variation by the PMU rotor using a Hall sensor. Hall sensor can output the voltage which has one-to-one correspondence with the magnetic field. This voltage is the electromotive force produced by the Hall effect. The raw output
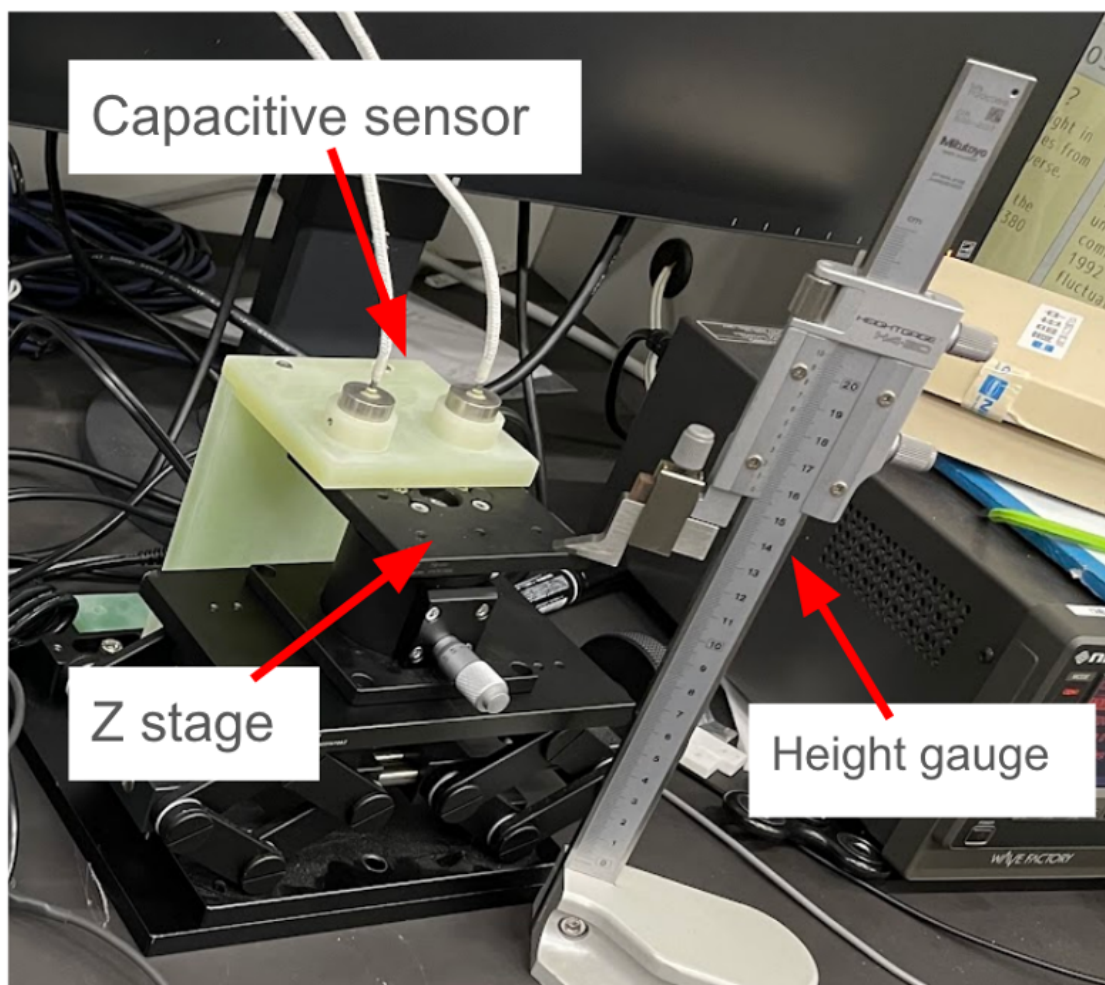
Figure4.1   The instruments for the calibration of the outputs of the capacitive sensor.
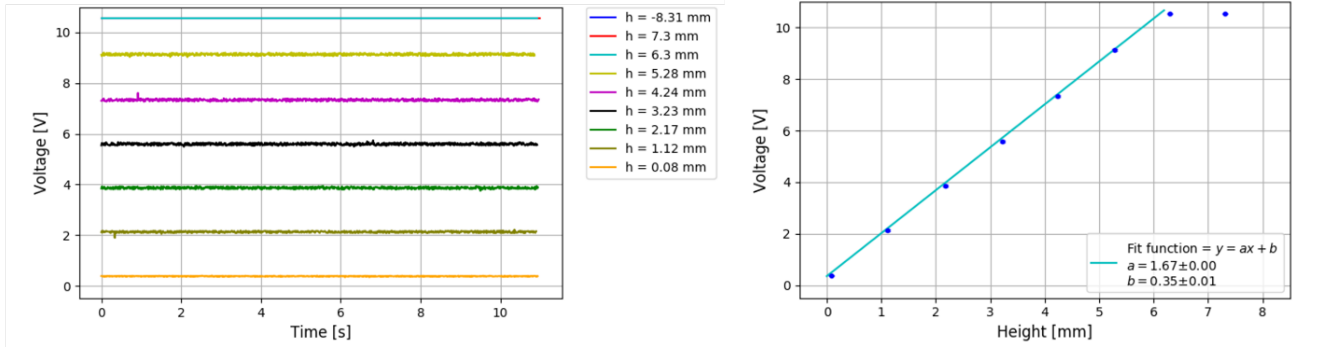
Figure4.2　Left: the output voltage of the capacitive sensor in each measured elevation of the Z stage which moved down. Right: the mean voltage in each measured elevation. This result is one example in 10 trials.
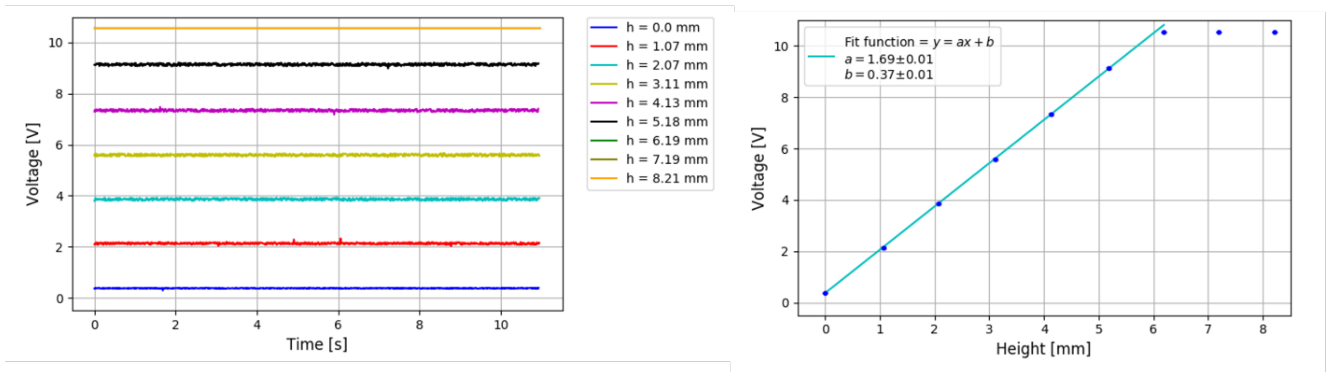
Figure4.3　Left: the output voltage of the capacitive sensor in each measured elevation of the Z stage which moved up. Right: the mean voltage in each measured elevation. This result is one example in 10 trials.

voltage of the Hall sensor is converted to the magnetic field by the Lake Shore Model 425 Gaussmeter. We monitor the magnetic field with the Gaussmeter.

These measurement results are used to evaluate the vibration of the PMU rotor. We set the capacitive sensor whose bottom surface becomes parallel to the top surface of the encoder disc. And we insert the Hall sensor in the space between the bottom surface of the PMU rotor and the top surface of the HTS.

4.3　Experiment

Before cooling the PMU stator, the PMU rotor is held by three cryogenic holding mechanisms (Figure 2.8) at a distance of 5 mm from the PMU stator. The HTS of the
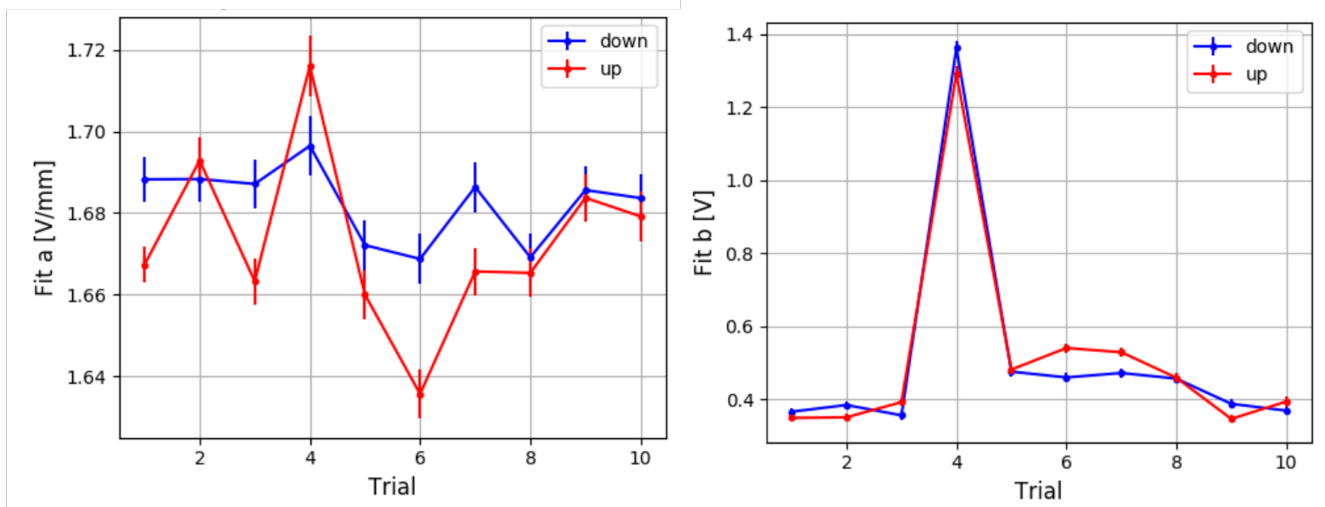
Figure4.4 Left: the inclinations by the linear fitting in the relation between the mean voltages of the capacitive sensor and the elevations. Right: the interceptions by the fitting results.

PMU stator are submerged in liquid nitrogen (LN2). Once the HTS has the temperature below the critical temperature, the cryogenic holder mechanisms releases the PMU rotor. The PMU rotor is free to levitate and can rotate in azimuth. The LN2 level is kept below the level which the PMU rotor does not has the friction with the LN2.

We tested the measurements of the vibration effects in four states of the PMU rotor; 1) the state that the PMU rotor is held by the cryogenic holder mechanisms, 2) the state that the PMU rotor is free to levitate, 3) the state that the PMU rotor is free to levitate and we tap the PMU rotor horizontally and vertically by a hammer, and 4) the stable rotation state. We expect there are horizontal and vertical natural vibrations when the PMU rotor is free (58) to levitate. The measurement of state 1 and state 2 with the capacitive sensor and the Hall sensor reveals whether the levitating PMU rotor has natural vibrations. The measurement of state 2 reveals the natural frequency of each vibration. In state 3, we rotate the PMU rotor at the stable rotation frequency, 1 Hz. We let it rotates for 10 minutes with monitoring the rotational speed by using optical encoders, and the vibration by a Hall sensor and a capacitive sensor. All the data are obtained simultaneously to discuss the correlation of them.

4.4 Result

Figure 4.5 shows the time-ordered data of the Hall sensor and the capacitive sensor when the PMU rotor is in state 1 (blue) and state 2 (orange). The peaks in the data of the Hall sensor are shown when the Hall sensor is not placed between the permanent magnet ring and the HTS ring. This is an artifact due to a mismatch of the data acquisition rate of the Gaussmeter and sampling rate of the multiple channel analyzer. Therefore, we ignore these peaks.
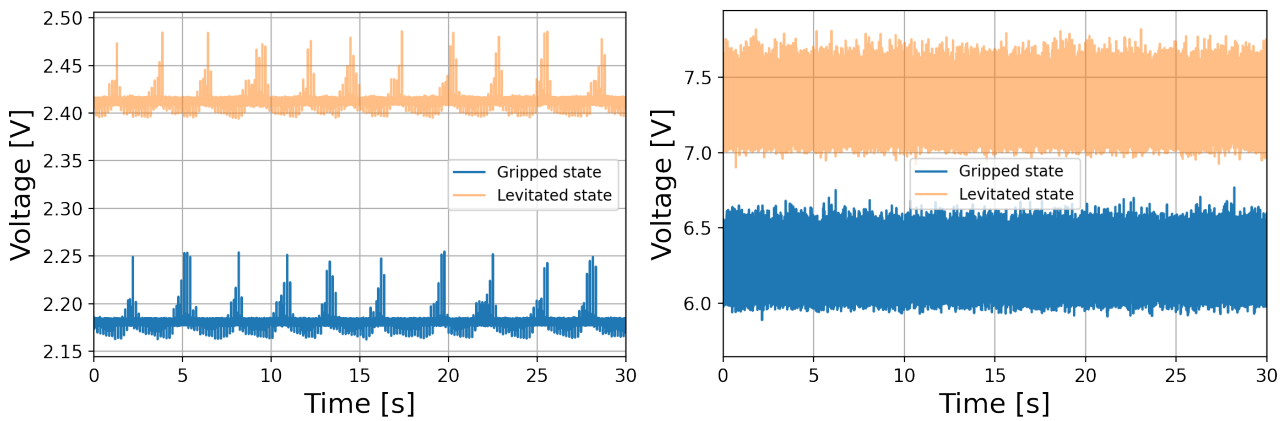
Figure4.5   The time-order data of the Hall sensor (left) and the capacitive sensor (right) when the PMU rotor is gripped by the holding mechanism and levitated. Figures are based on the study of (17).

The left panel of Figure 4.6 shows the power spectrum density (PSD) of the magnetic field measured by the Hall sensor when the PMU rotor is held and levitated. And the right panel of Figure 4.6 shows a closeup view of the left panel in the frequency range from 1 Hz to 100 Hz. There are two broad peaks in the PSD of the magnetic field at 8 Hz and 15 Hz only when the PMU rotor is levitated. These peaks correspond to the natural frequencies in radial direction and axial direction, and these are consistent with previously reported peak locations (58). We also observe peaks above 20 Hz when the PMU rotor is held and levitated. We attribute these to spurious effects due to the evaporation of LN2 in the vicinity of the Hall sensor. Furthermore, the outputs of the Hall sensor is read by a Lakeshore Gauss meter which filters above 400 Hz. Therefore, we do not investigate the causes of peaks at higher frequency beyond this cut-off frequency.
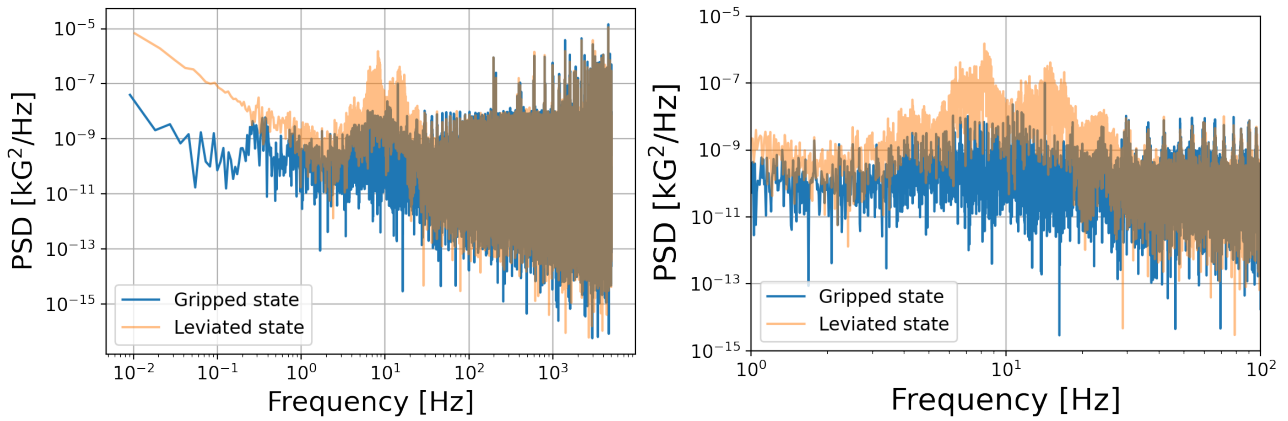
Figure4.6   Left: the PSD of the magnetic field between the SMB permanent magnets and the high temperature superconductors when the PMU rotor was gripped (blue) and levitated (orange). Right: the zoomed plot from 1 Hz to 100 Hz of each PSD. Figures are based on (17).
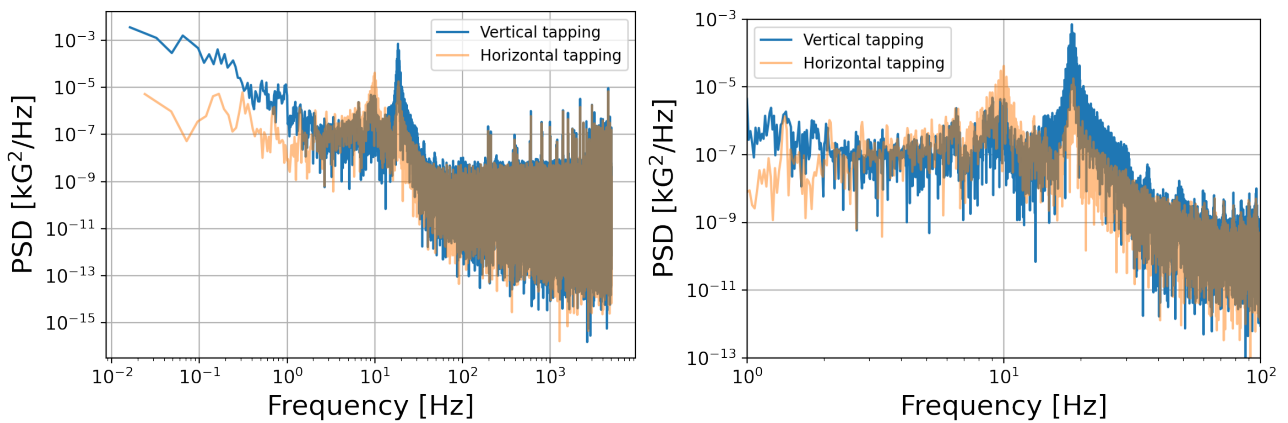
Figure4.7   Left: the PSD of the magnetic field between the SMB permanent magnets and the high temperature superconductors when we tap the PMU rotor vertically (blue) and horizontally (orange). Right: the zoomed plot from 1 Hz to 100 Hz of each PSD. Figures are based on the study (17).

Figure 4.7 shows the PSDs of the magnetic field when we tap the PMU rotor vertically and horizontally. The plots show the lower frequency corresponds to the vibration in radial direction and the higher one corresponds to the vibration in axial direction. The frequencies at both peaks are consistent with the frequencies shown in Figure 4.6.

Figure 4.8 shows the PSD of the outputs of the Hall sensor and the capacitive sensor when the PMU rotor rotates at 1 Hz. Assuming outputs of the capacitive sensor is only caused

by the vertical displacement, the output voltage is converted to the vertical displacement of the PMU rotor according to Equation 4.1. Both PSDs show distinctive peaks at the rotational frequency of 1 Hz and its harmonics. The most prominent peak in the capacitive
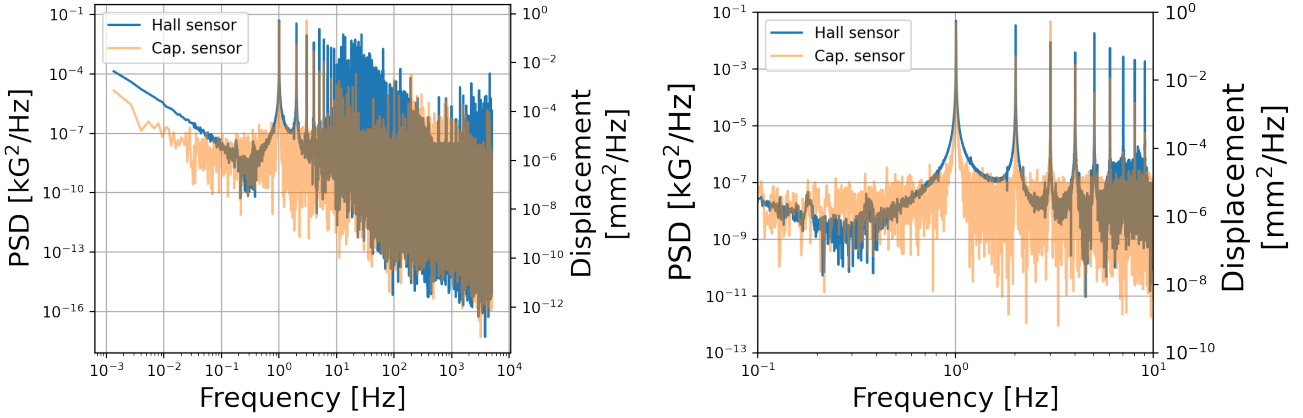
Figure4.8 Left: the PSD of the Hall sensor output (blue) and the capacitive sensor output (orange) when the PMU rotor was spun at 1 Hz. Right: the zoomed plot from 0.1 Hz to 10 Hz of the left panel. Figures are based on (17).

sensor PSD is observed at 1 Hz. The observed power corresponds to result shows the physical displacement amplitude of $36\,\mu\mathrm{m}$ at 1 Hz. The vertical displacement is a change in physical distance between the capacitive sensor and the encoder disc. It is likely to caused by the axial vibration of the rotor, since the encoder disc itself can be regard rigid at this low frequency. Thus, we assume this value, $36\,\mu\mathrm{m}$, is the upper limit of the amplitude of physical displacement by the mechanical vibration. Note that we need to consider up to the harmonics and broadness of all peaks to discuss the vibrations, but we focus on the peak value in the rotation frequency, 1Hz, for simplicity in this thesis.

Figure 4.9 shows the peak profile of fourth harmonic to characterize the vibration of the PMU rotor. This peak is consistent with Lorentzian, i.e. a power of forced oscillation with an attenuation $P(f)$, shown as

$$P(f) = \frac{F_0^2}{4\pi^2((f - f_0)^2 + (2\gamma f_0))^2},$$
(4.2)

where F_0 is an amplitude of forced oscillation, f_0 is a center frequency, and γ is an attenuation coefficient. Each best-fit parameter is 2.5×10^{-4}, 4.02 Hz, and 2.7×10^{-9}, respectively. The corresponding width is parameterized by a Q-value equal to 3×10^7.
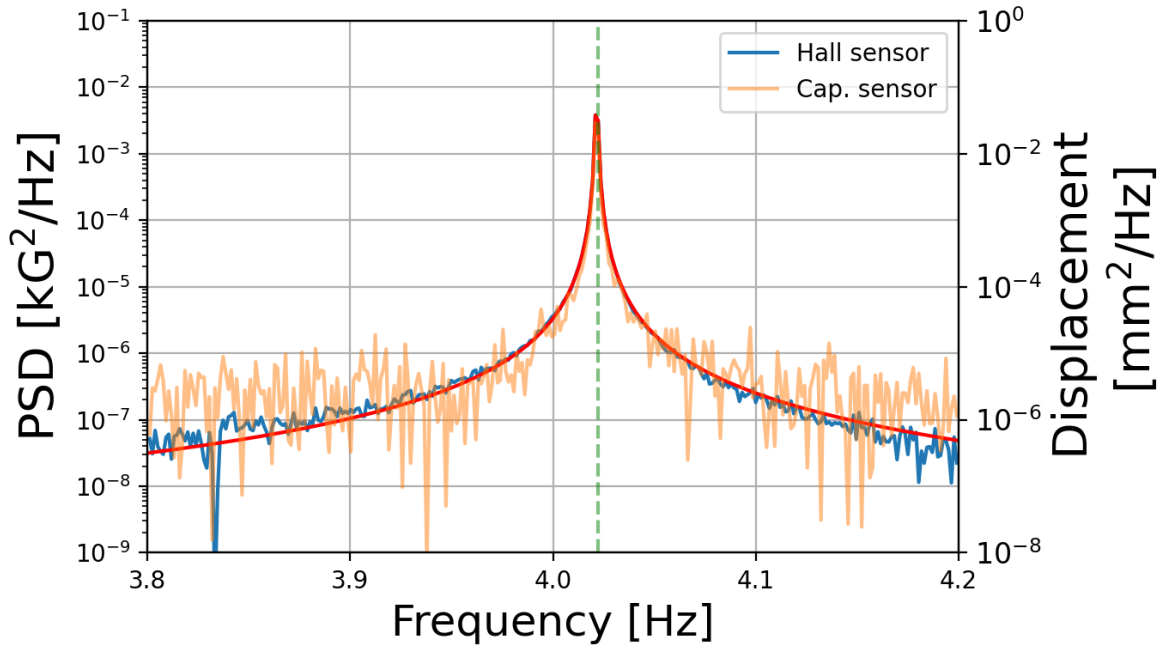
Figure4.9   Closeup view of the frequency region from 3.8 Hz to 4.2 Hz in Fig. 4.8 shows around the fourth harmonic peak of the rotational frequency. We used the Hall sensor instead of the capacitive sensor to fit because the Hall sensor has a better sensitivity. We assume the magnetic field and the displacement is proportional to each other within the displacement less than 1 mm. This figure is based on (17).

4.5   Discussion

In this section, we discuss two potential effects originated from the PMU rotor vibration; 1) a propagation of the magnetic field due to the permanent magnet in the PMU rotor, and 2) a propagation of mechanical forces by the rotor vibration. In this discussion, we use the current design of the LiteBIRD LFT configuration to define the relative position between the HWP and the focal plane (10). We also assume that the PMU rotor has the maximum amplitude of 36 μm.

Variation of the magnetic field

We simulate the magnetic field at the focal plane due to the vibration of the PMU rotor magnet by using a commercially available finite element magnetic simulation software,
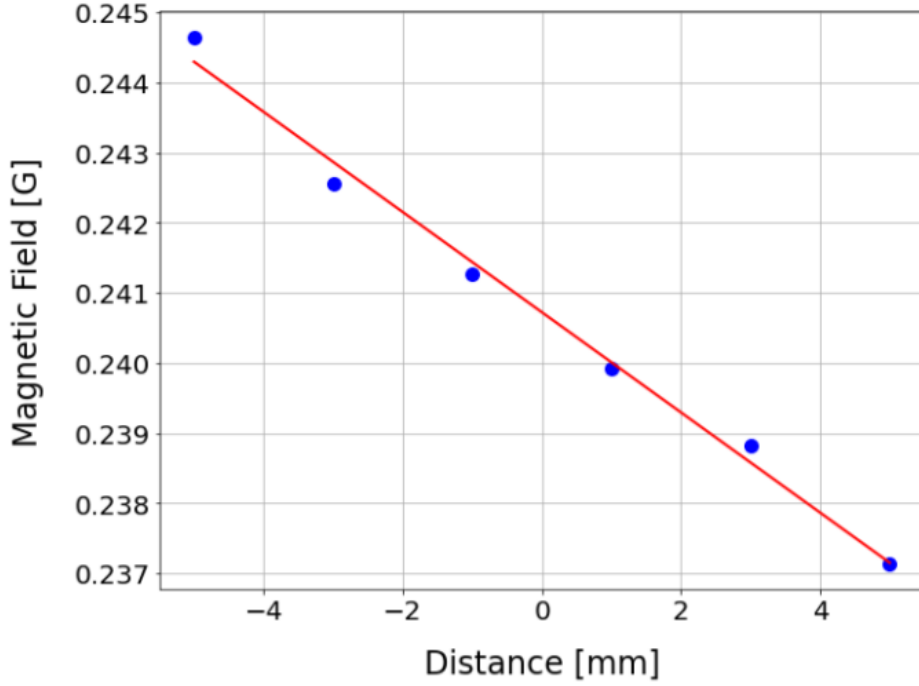
Figure4.10   The simulated magnetic field of the rotor at the center of the focal plane as a function of rotor displacement along the optical axis. We vary the permanent magnet ring axially along the optical axis, and map the magnitude of the magnetic field. This figure is based on (17).

JMAG (59). Due to the result of the simulation (Figure 4.10), we find the static magnetic field and the fluctuations of magnetic field in the focal plane of 0.24 G and 3×10^{-5} G in amplitude, respectively. The development of LiteBIRD TES bolometers are in progress, therefore we use literature values for the magnetic field susceptibility of ground-base experiments TESes. The prior research (60) reported a quadratic relationship shown as

$$T_c = wB_{ext}^2, \tag{4.3}$$

where the critical temperature of the TES bolometer, T_c, the external magnetic field, B_{ext}, and the sensitivity coefficient w. We apply the highest sensitivity coefficient found in this study, which corresponds to $w = 4.6 \times 10^{-3}$ K/G^2 from MoCu based TES designed for ACTpol. For a conservative estimation due to the small applied magnetic field, we expand Equation 4.3 by the Taylor expansion (61; 62), shown as

$$\Delta T_c \sim \frac{dT_c}{dB_{ext}}\bigg|_{B_{ext}} \Delta B_{ext} = 2wB_{ext}\Delta B_{ext}. \tag{4.4}$$

As a result, ΔT_c becomes 7×10^{-8} K.

In LiteBIRD, the outputs of the TES array is read by a Superconducting QUantum Interference Device (SQUID) which is sensitive to magnetic fields. And, LiteBIRD utilizes a frequency domain digital multiplexing (DfMUX) readout system (63). DfMUX has been used by recent CMB experiment, such as POLARBEAR-2 and SPT-3G. Luker et al. (64) reported the susceptibility of SQUIDs to external magnetic fields. Assuming a similar magnetic shielding scheme, the relationship between the fractional flux change and the external AC magnetic field B_{ext} is shown as

$$\delta\Phi/\Phi_0 = 0.06 + 1.03 B_{ext}. \tag{4.5}$$

This results in a fractional flux $\delta\Phi/\Phi_0|_{ac} = 3.1 \times 10^{-5}$. This test was carried out with a non-gradiometric base SQUID fabricated at NIST. The new-generation SQUIDs should be less sensitive to external magnetic fields. Therefore, the shown result should be regarded as an upper limit.

Mechanical vibration

Mechanical vibrations of the PMU rotor will propagate to the detector system. The detailed propagation mechanism in a cryogenically cooled structure is beyond the scope of this thesis, nevertheless, we can compare a similar situation with the PMU rotor vibration. If we assume the vibration of the PMU rotor as the simple harmonic oscillation, the force F can be defined as

$$F = m\ddot{x} = mA(2\pi f)^2 \sin{(2\pi f t)}, \tag{4.6}$$

where m is the rotor mass, A is the vibration amplitude, and f is the vibration frequency. In this equation, we assume m = 25 kg, A = 36 μm, and f = at 1 Hz as representative values. Thus, the resultant force due to the vibration is estimated to be 3.6×10^{-2} N. The prior study reported on the measured force produced by a space qualified 1 K Joule Thomson cooler (65). The maximum value is found at the driving frequency of 40 Hz, which is in the range $0.1 \sim 10$ N depending on the orientation and the cooler. The vibration force of the PMU rotor is estimated to be comparable or smaller than the value of the cooler. Again, further assessment of implication of this value is left for future analysis.

Chapter 5.

Further steps for development of LFT PMU engineering/flight model

We discussed the performances of the prototype of the LFT PMU and their scientific implications in the sections so far. In this section, we discuss further steps required for the development of the engineering model and the flight model (EM/FM) of the LFT PMU.

5.1 Requirements

Table 2.9 shows current design guidances of the EM/FM of the LFT PMU. Majority of design guidances are set as same values of the prototype, and examples of the targets are explained in Section 2.5.

The different values between the prototype and the EM/FM are the effective area of the HWP and the total mass of the PMU. The prototype of the LFT PMU is a semi-real size model assuming a diameter of the HWP as 330 mm. On the other hand, the diameter of the HWP used in the EM/FM will be ≥ 400 mm. And, the EM/FM design of LFT PMU will be updated to reduce the total mass.

The development of the EM/FM will be entrusted to satellite development companies after all evaluations of the prototype PMU. The further sections show the required evaluation items and further steps for the development of the EM/FM.

5.2   Further evaluations for angular encodings

In Section 3, we evaluate the angular error of the HWP by using the raw periods of encoder signals when the prototype of the LFT PMU rotor rotates at 1 Hz. In this process, we adopt two assumptions; 1) we calculate the angular error without any process, such as down-sampling of the HWP angles, and 2) we measure not only the period but also absolute times simultaneously when the encoder signal is triggered.

Assuming the rotational frequency f_{rot} is constant and trigger timings of the encoder signal are equispaced, the sampling rate of reconstructed angles f_s in our reconstruction method is

$$f_s = i_s \times f_{rot} \tag{5.1}$$

where i_s is a number of slots in the encoder disc. Therefore, each angle is expected as $2.81°$ because the number of slots i_s is 128 in the prototype and the rotation frequency f_{rot} is 1 Hz in the experiment. Higher sampling rate is ideal in terms of the angle resolution of the HWP. However, we need to do the down-sampling of the angles, which is the method to summarize the angles to lower samples, to match the sampling rate of the modulated signal. Current target rate is set as 19 Hz. The official error of reconstructed angles with all process is beyond the scope of this thesis.

We calculated periods of the encoder signal for the reconstruction of angles in each slot. A reconstruction of the HWP angle will need a cumulative sum of calculated angles in a range of $0°$ to $360°$. Identically, an error in HWP angles should be accumulated for the cumulative reconstructed angles. To avoid the accumulation of the error, we require the absolute timestamps when the encoder signal is triggered.

Above two points are essential to take measures in further steps.

5.3   Rotational stability

A duration of the operation of LiteBIRD is expected for three years. Ideally, the rotation of the HWP will be continued for the same duration. Then, we must prove the rotation has the enough stability for three years. This requires longer duration experiment than 10 min which is set as the experiment duration in this thesis, therefore, this experiment should be

done in 4K GM cryostat. This thesis leaves this content out of scope.

5.4   Characterization of heat dissipation

A heat dissipation in the LFT PMU produces a thermal noise mixed in the observed CMB signal. The current design guidance of the total heat dissipation given off by the LFT PMU is set as 4 mW. Possible origins of the LFT PMU are mainly three; 1) LED used in optical encoders, 2) coils of brush-less motor in the PMU stator, and 3) the SMB (this is shown in Section 2.6).

The LED is a semiconductor which gives off the light when the enough current is applied. This is activated by the constant current, and we use 10 mA tentatively. The voltage applied in the LED is ∼1.3 V at room temperature, and ∼1.7 V in LN2 experiment. The prototype adopts three encoders, therefore, the heat dissipation of the LED becomes 51 mW in the LN2 experiment. To reduce this heat dissipation, we will find the minimum currents used in LEDs. In the future analysis, we need the estimation of minimum constant currents in LEDs that can be used for the reconstruction of the HWP angle and satisfies the requirement of the heat dissipation.

Coils are components of the brush-less motor in the PMU stator. This simply consists of three conductors, called U, V, and W phase. The resistance values of three combinations using U, V, and W phase are ∼25 Ω at room temperature and ∼16 Ω in liquid nitrogen. An amplitudes of three-phase currents are able to be controlled by the motor driver produced by Asahi Engineering Company. The rotation experiment shown in chapter 4 employs the initial current amplitude of 20 mA, while the minimum current is 10 mA for the continuous rotation at 1 Hz. Therefore, the total heat dissipation in three-phase coils becomes at most 4.8 mW in liquid nitrogen experiment and at 1 Hz rotation. This is close to the total design guidance of the heat dissipation in the LFT PMU, 4 mW. The further reduction of this heat is expected in the updated design of the LFT PMU in the future.

5.5   Integration test of LFT

The PMU for LiteBIRD LFT is under the development of the prototype of the semi-real size rotation mechanism, the semi-real size HWP, and the test model of TES bolometers.

Their prototypes are independently evaluated in each experiment to measure several performances and systematic effects. In this process, we identify problems in the prototype designs.

The performances of new model of the rotation mechanism is still being tested. The semi-real size HWP will be mounted at the center of the rotation mechanism. The HWP has been independently validated at least for these four items; 1) a bonding material selection of the multiple sapphire plates to endure a force at the launch (66; 67), 2) an optimization of combinations of optical axes of sapphire plates to maximize the modulation efficiency (13), 3) a transmittance due to a laser processing at the surfaces of the HWP (14) , and 4) systematic effects by the incident angle and off-axes of sapphire plates.

Finally and as the future analyses, all prototype instruments for the LFT will be integrated to analyze the performances and systematics comparing each independent experiment result. Especially, we will be able to understand optical performances of the prototype of the LFT, and the effects of systematics, such as magnetic fields of the rotation mechanism to TES detectors, to the optical signal. Magnetic fields of the rotation mechanism will be proportional to the inverse of squared distances between the rotation mechanism and TES detectors. Such effect is thought as the noise source in TES detectors. Also, the LFT has a lot of other instruments, such as the mirrors to connect the optical source, the LFT PMU, and TES detectors, and windows used in 4K GM cryostat and ADR. All systematics will be shown in the modulation signal, and which should be disassembled in each origin.

Chapter 6.

Summary

CMB is the isotropic blackbody radiation at 2.725 K and can be observed in full-sky. The detection of the CMB is a smoking gun of Big-Bang in the early Universe. Several experiments observe the CMB for decades, and the results have established modern cosmology. Recently, the linear polarization of the CMB has received a lot of attention for the validation of inflation theories. The theories proposes the models of an exponential expansion which would happen in the initial Universe. The rapid expansion has been expected to produce primordial gravitational waves, which can be the only communicator in the era before the clearing up of the Universe. When this has produced the quadrupole of the CMB anisotropy, it is expected to observe two patterns of the CMB linear polarization, called E-mode and B-mode. Since E-mode can be produced by density fluctuations in the early Universe, the detection of this primordial B-mode proves the inflation theory.

The next generation satellite, LiteBIRD, is one of the satellites which aims to observe this B-mode. LiteBIRD is the JAXA/ISAS strategic large class satellite mission and observes full-sky from the second Lagrange point (L2). There are three frequency range telescopes, called Low, Middle, and High-Frequency Telescope (LFT/MFT/HFT). All telescopes adopt polarization modulator units (PMU), which are the instruments to rotate a half-wave plate (HWP) continuously, to reduce a 1/f noise and systemic effects by the performance difference of orthogonal detectors. The LFT PMU will adopt a brushless motor and a superconducting magnetic bearing to realize a contact-less rotation of the PMU rotor.

In this thesis, we evaluate critical performances of the prototype of the LFT PMU

developed for the next generation CMB observation satellite LiteBIRD.

First, we evaluated the reconstruction method and the results of position angles of the HWP. This angle has a correspondence with the incident polarization angle which is used for the demodulation of observation signals. The accuracy of reconstructed angles depends on the leakage of E-mode into B-mode. The estimated accuracy is 2.48×10^{-1} arcmin, which satisfies the design guidance value of 0.5 arcmin. We describe the potential sources giving the contribution into the error of position angles, and quantify all expected contributions. Finally, we show the root mean square of all error components is consistent with the the angular accuracy due to the measured periods.

We also evaluate potential effects of the vibration of the LFT PMU rotor. The prototype of the PMU realizes the contact-less rotation, on the other hand, we anticipate the PMU rotor has horizontal and vertical vibration due to the SMB system. We measured the vertically physical displacement of the PMU rotor using a Hall sensor and a capacitive sensor in stable rotation at 1 Hz. Through this experiment, we showed the displacement of the PMU rotor becomes 36 μm. Based on this displacement, we evaluated two expected effects due to the vibration of the PMU rotor, and we described the potential impact on the low-temperature detector system.

Reference

[1] https://www.flickr.com/photos/nasacommons/16315677368/in/photolist-qRL7sd.

[2] https://science.nasa.gov/missions/cobe.

[3] DJ Fixsen, ES Cheng, JM Gales, John C Mather, RA Shafer, and EL Wright. The cosmic microwave background spectrum from the full cobe* firas data set. *The Astrophysical Journal*, 473(2):576, 1996.

[4] http://www.astro.ucla.edu/~wright/cosmo_01.htm.

[5] WMAP collaboration et al. Seven-year wilkinson microwave anisotropy probe (wmap) observations: cosmological interpretation. *Astrophys. J. Suppl*, 192(18):1001–4538, 2011.

[6] Nabila Aghanim, Yashar Akrami, Frederico Arroja, Mark Ashdown, J Aumont, Carlo Baccigalupi, M Ballardini, Anthony J Banday, RB Barreiro, Nicola Bartolo, et al. Planck 2018 results-i. overview and the cosmological legacy of planck. *Astronomy & Astrophysics*, 641:A1, 2020.

[7] https://www.cosmos.esa.int/web/planck/picture-gallery.

[8] Masashi Hazumi, Peter AR Ade, Alexandre Adler, Erwan Allys, David Alonso, Kam Arnold, Didier Auguste, Jonathan Aumont, Ragnhild Aurlien, Jason Austermann, et al. Litebird satellite: Jaxa's new strategic l-class mission for all-sky surveys of cosmic microwave background polarization. In *Space Telescopes and Instrumentation 2020: Optical, Infrared, and Millimeter Wave*, volume 11443, page 114432F. International Society for Optics and Photonics, 2020.

[9] Hajime Sugai, PAR Ade, Y Akiba, D Alonso, K Arnold, J Aumont, J Austermann, Carlo Baccigalupi, Anthony J Banday, Ranajoy Banerji, et al. Updated design of the cmb polarization experiment satellite litebird. *Journal of Low Temperature Physics*,

199(3):1107–1117, 2020.

[10] Yutaro Sekimoto, Peter Ade, Kam Arnold, Jonathan Aumont, Jason Austermann, Carlo Baccigalupi, Anthony Banday, Ranajoy Banerji, Soumen Basak, Shawn Beckman, et al. Concept design of the litebird satellite for cmb b-mode polarization. In *Space Telescopes and Instrumentation 2018: Optical, Infrared, and Millimeter Wave*, volume 10698, page 106981Y. International Society for Optics and Photonics, 2018.

[11] Yuki Sakurai, Tomotake Matsumura, Nobuhiko Katayama, Kunimoto Komatsu, Ryota Takaku, Shinya Sugiyama, Yoshiki Nomura, Takayuki Toda, Tommaso Ghigna, Teruhito Iida, et al. Breadboard model of the polarization modulator unit based on a continuously rotating half-wave plate for the low-frequency telescope of the litebird space mission. In *Millimeter, Submillimeter, and Far-Infrared Detectors and Instrumentation for Astronomy X*, volume 11453, page 114534E. International Society for Optics and Photonics, 2020.

[12] Shivaramakrishnan Pancharatnam. Achromatic combinations of birefringent plates. In *Proceedings of the Indian Academy of Sciences-Section A*, volume 41, pages 137–144. Springer, 1955.

[13] Kunimoto Komatsu, Hirokazu Ishino, Nobuhiko Katayama, Tomotake Matsumura, Yuki Sakurai, and Ryota Takaku. Design of the frequency independent optic axis of the pancharatnam base achromatic half-wave plate for cmb polarization experiment. In *Millimeter, Submillimeter, and Far-Infrared Detectors and Instrumentation for Astronomy X*, volume 11453, page 114534B. International Society for Optics and Photonics, 2020.

[14] Ryota Takaku, S Hanany, H Imada, H Ishino, N Katayama, K Komatsu, K Konishi, M Kuwata-Gonokami, T Matsumura, K Mitsuda, et al. Broadband, millimeter-wave anti-reflective structures on sapphire ablated with femto-second laser. *Journal of Applied Physics*, 128(22):225302, 2020.

[15] Kunimoto Komatsu, Tomotake Matsumura, Hiroaki Imada, Hirokazu Ishino, Nobuhiko Katayama, and Yuki Sakurai. Demonstration of the broadband half-wave plate using the nine-layer sapphire for the cosmic microwave background polarization experiment. *Journal of Astronomical Telescopes, Instruments, and Systems*, 5(4):044008, 2019.

[16] A Kusaka, T Essinger-Hileman, JW Appel, P Gallardo, KD Irwin, N Jarosik, MR Nolta, LA Page, LP Parker, S Raghunathan, et al. Modulation of cosmic microwave background polarization with a warm rapidly rotating half-wave plate on the atacama b-mode search instrument. *Review of Scientific Instruments*, 85(2):024501, 2014.

[17] S Sugiyama et al. Vibration characteristics of a continuously rotating superconducting magnetic bearing and potential influence to tes and squid. *Journal of Low Temperature Physics*. DOI: 10.1007/s10909-022-02846-1.

[18] Shinya Sugiyama, Tomotake Matsumura, Yuki Sakurai, Nobuhiko Katayama, Satoru Takakura, Makoto Tashiro, Yukikatsu Terada, Kosuke Sato, Satoru Katsuda, Yurika Hoshino, et al. Evaluation of reconstructed angular error of a continuous rotating hwp for litebird. In *Space Telescopes and Instrumentation 2020: Optical, Infrared, and Millimeter Wave*, volume 11443, pages 1099–1112. SPIE, 2020.

[19] Ralph A Alpher, Hans Bethe, and George Gamow. The origin of chemical elements. *Physical Review*, 73(7):803, 1948.

[20] George Gamow. Expanding universe and the origin of elements. *Physical review*, 70(7-8):572, 1946.

[21] Arno A Penzias and Robert Woodrow Wilson. A measurement of excess antenna temperature at 4080 mc/s. *The Astrophysical Journal*, 142:419–421, 1965.

[22] Nancy W Boggess, John C Mather, R Weiss, Charles L Bennett, ESe al Cheng, E Dwek, S Gulkis, Michael G Hauser, Michael A Janssen, T Kelsall, et al. The cobe mission-its design and performance two years after launch. *The Astrophysical Journal*, 397:420–429, 1992.

[23] John C Mather, ES Cheng, David A Cottingham, RE Eplee Jr, Dale J Fixsen, Tilak Hewagama, RB Isaacman, KA Jensen, Stephan S Meyer, Peter D Noerdlinger, et al. Measurement of the cosmic microwave background spectrum by the cobe firas instrument. *The Astrophysical Journal*, 420:439–444, 1994.

[24] Martin White, Douglas Scott, and Joseph Silk. Anisotropies in the cosmic microwave background. *Annual Review of Astronomy and Astrophysics*, 32(1):319–370, 1994.

[25] Wayne Hu and Scott Dodelson. Cosmic microwave background anisotropies. *Annual Review of Astronomy and Astrophysics*, 40(1):171–216, 2002.

[26] Anthony Challinor and Hiranya Peiris. Lecture notes on the physics of cosmic microwave background anisotropies. In *AIP Conference Proceedings*, volume 1132, pages 86–140. American Institute of Physics, 2009.

[27] J Dunkley, Eiichiro Komatsu, MR Nolta, DN Spergel, D Larson, G Hinshaw, L Page, CL Bennett, B Gold, N Jarosik, et al. Five-year wilkinson microwave anisotropy probe* observations: Likelihoods and parameters from the wmap data. *The Astrophysical Journal Supplement Series*, 180(2):306, 2009.

[28] Gary Hinshaw, D Larson, Eiichiro Komatsu, David N Spergel, CLaa Bennett, Joanna Dunkley, MR Nolta, M Halpern, RS Hill, N Odegard, et al. Nine-year wilkinson microwave anisotropy probe (wmap) observations: cosmological parameter results. *The Astrophysical Journal Supplement Series*, 208(2):19, 2013.

[29] Charles L Bennett, Davin Larson, Janet L Weiland, N Jarosik, G Hinshaw, N Odegard, KM Smith, RS Hill, B Gold, M Halpern, et al. Nine-year wilkinson microwave anisotropy probe (wmap) observations: final maps and results. *The Astrophysical Journal Supplement Series*, 208(2):20, 2013.

[30] J Colin Hill, Erminia Calabrese, Simone Aiola, Nicholas Battaglia, Boris Bolliet, Steve K Choi, Mark J Devlin, Adriaan J Duivenvoorden, Jo Dunkley, Simone Ferraro, et al. The atacama cosmology telescope: Constraints on pre-recombination early dark energy. *arXiv preprint arXiv:2109.04451*, 2021.

[31] D Hanson, S Hoover, A Crites, PAR Ade, KA Aird, JE Austermann, JA Beall, AN Bender, BA Benson, LE Bleem, et al. Detection of b-mode polarization in the cosmic microwave background with data from the south pole telescope. *Physical review letters*, 111(14):141301, 2013.

[32] JT Sayre, CL Reichardt, JW Henning, PAR Ade, AJ Anderson, JE Austermann, JS Avva, JA Beall, AN Bender, BA Benson, et al. Measurements of b-mode polarization of the cosmic microwave background from 500 square degrees of sptpol data. *Physical Review D*, 101(12):122003, 2020.

[33] Matias Zaldarriaga and Uroš Seljak. All-sky analysis of polarization in the microwave background. *Physical Review D*, 55(4):1830, 1997.

[34] Marc Kamionkowski, Arthur Kosowsky, and Albert Stebbins. Statistics of cosmic microwave background polarization. *Physical Review D*, 55(12):7368, 1997.

[35] Matias Zaldarriaga and Uroš Seljak. All-sky analysis of polarization in the microwave background. *Physical Review D*, 55(4):1830, 1997.

[36] Joshua N Goldberg, Alan J MacFarlane, Ezra T Newman, Fritz Rohrlich, and EC George Sudarshan. Spin-s spherical harmonics and . *Journal of Mathematical Physics*, 8(11):2155–2161, 1967.

[37] Josquin Errard, Peter AR Ade, A Anthony, K Arnold, F Aubin, D Boettger, J Borrill, C Cantalupo, MA Dobbs, D Flanigan, et al. The new generation cmb b-mode polarization experiment: Polarbear. *arXiv preprint arXiv:1011.0763*, 2010.

[38] PAR Ade, Y Akiba, AE Anthony, K Arnold, M Atlas, D Barron, D Boettger, J Borrill, S Chapman, Y Chinone, et al. A measurement of the cosmic microwave background b-mode polarization power spectrum at sub-degree scales with polarbear. *The Astrophysical Journal*, 794(2):171, 2014.

[39] Peter AR Ade, RW Aikin, D Barkats, SJ Benton, CA Bischoff, JJ Bock, JA Brevik, I Buder, E Bullock, CD Dowell, et al. Detection of b-mode polarization at degree angular scales by bicep2. *Physical Review Letters*, 112(24):241101, 2014.

[40] PAR Ade, Z Ahmed, RW Aikin, Kate Denham Alexander, D Barkats, SJ Benton, Colin A Bischoff, JJ Bock, R Bowens-Rubin, JA Brevik, et al. Bicep2/keck array viii: Measurement of gravitational lensing from large-scale b-mode polarization. *The Astrophysical Journal*, 833(2):228, 2016.

[41] Matias Zaldarriaga and Uroš Seljak. Gravitational lensing effect on cosmic microwave background polarization. *Physical Review D*, 58(2):023003, 1998.

[42] Samuel M Leach, J-F Cardoso, Carlo Baccigalupi, RB Barreiro, M Betoule, J Bobin, A Bonaldi, J Delabrouille, G De Zotti, C Dickinson, et al. Component separation methods for the planck mission. *Astronomy & Astrophysics*, 491(2):597–615, 2008.

[43] Mathieu Remazeilles, Anthony J Banday, Carlo Baccigalupi, S Basak, A Bonaldi, G De Zotti, J Delabrouille, C Dickinson, HK Eriksen, J Errard, et al. Exploring cosmic origins with core: B-mode component separation. *Journal of Cosmology and Astroparticle Physics*, 2018(04):023, 2018.

[44] R. W. Ogburn IV et al. The bicep2 cmb polarization experiment. *Proceedings of SPIE Astronomical Telescopes + Instrumentation: High Energy, Optical, and Infrared Detectors for Astronomy IV*, 7741, 2010.

[45] Marc Kamionkowski and Ely D Kovetz. The quest for b modes from inflationary gravitational waves. *Annual Review of Astronomy and Astrophysics*, 54:227–269, 2016.

[46] PAR Ade, Z Ahmed, M Amiri, D Barkats, R Basu Thakur, CA Bischoff, D Beck, JJ Bock, H Boenish, E Bullock, et al. Improved constraints on primordial gravitational waves using planck, wmap, and bicep/keck observations through the 2018 observing season. *Physical Review Letters*, 127(15):151301, 2021.

[47] Matias Zaldarriaga. Polarization of the microwave background in reionized models. *Physical Review D*, 55(4):1822, 1997.

[48] Brandon S Hensley and Philip Bull. Mitigating complex dust foregrounds in future cmb polarization experiments. *arXiv preprint arXiv:1709.07897*, 2017.

[49] Yashar Akrami, M Ashdown, Jonathan Aumont, Carlo Baccigalupi, M Ballardini, Anthony J Banday, RB Barreiro, Nicola Bartolo, S Basak, K Benabed, et al. Planck 2018 results-iv. diffuse component separation. *Astronomy & Astrophysics*, 641:A4, 2020.

[50] Kunimoto Komatsu, Hirokazu Ishino, Hirokazu Kataza, Kuniaki Konishi, Makoto Kuwata-Gonokami, Nobuhiko Katayama, Shinya Sugiyama, Tomotake Matsumura, Haruyuki Sakurai, Yuki Sakurai, et al. Demonstration of five-layer phase-flat achromatic half-wave plate with anti-reflective structures and superconducting magnetic bearing for cmb polarization experiments. In *Millimeter, Submillimeter, and Far-Infrared Detectors and Instrumentation for Astronomy X*, volume 11453, page 114534I. International Society for Optics and Photonics, 2020.

[51] Ryota Takaku, Tomotake Matsumura, Haruyuki Sakurai, Kuniaki Konishi, Hiroaki Imada, Shaul Hanany, Karl Young, Qi Wen, Nobuhiko Katayama, Yuki Sakurai, et al. Demonstration of anti-reflective structures over a large area for cmb polarization experiments. In *Millimeter, Submillimeter, and Far-Infrared Detectors and Instrumentation for Astronomy X*, volume 11453, page 114531A. International Society for Optics and Photonics, 2020.

[52] Tomotake Matsumura. Mitigation of the spectral dependent polarization angle response for achromatic half-wave plate. *arXiv preprint arXiv:1404.5795*, 2014.

[53] Otto H Schmitt. A thermionic trigger. *Journal of Scientific instruments*, 15(1):24,

1938.

[54] Tomotake Matsumura, Shaul Hanany, John R Hull, Bradley Johnson, and Terry Jones. Magnetic field inhomogeneity and torque in high temperature superconducting magnetic bearings. *IEEE transactions on applied superconductivity*, 15(2):2316–2319, 2005.

[55] A Lewis, A Challinor, and A Lasenby. Efficient computation of cmb anisotropies in closed frw models, 2000. *Astrophys. J*, 538:473.

[56] Antony Lewis and Sarah Bridle. Cosmological parameters from cmb and other data: A monte carlo approach. *Physical Review D*, 66(10):103511, 2002.

[57] Alexei A Starobinsky. A new type of isotropic cosmological models without singularity. *Physics Letters B*, 91(1):99–102, 1980.

[58] Yuki Sakurai, Tomotake Matsumura, Hajime Sugai, Nobuhiko Katayama, Hiroyuki Ohsaki, Yutaka Terao, Yusuke Terachi, Hirokazu Kataza, Shin Utsunomiya, and Ryo Yamamoto. Vibrational characteristics of a superconducting magnetic bearing employed for a prototype polarization modulator. In *Journal of Physics: Conference Series*, volume 871, page 012091. IOP Publishing, 2017.

[59] JMAG : Simulation Technology for Electromechanical Design, http://www.jmag-international.com.

[60] EM Vavagiakis, SW Henderson, K Zheng, H-M Cho, NF Cothard, B Dober, SM Duff, PA Gallardo, G Hilton, J Hubmayr, et al. Magnetic sensitivity of almn teses and shielding considerations for next-generation cmb surveys. *Journal of Low Temperature Physics*, 193(3):288–297, 2018.

[61] Aritoki Suzuki. *Multichroic bolometric detector architecture for cosmic microwave background polarimetry experiments*. University of California, Berkeley, 2013.

[62] Tommaso Ghigna, Tomotake Matsumura, Masashi Hazumi, Samantha Lynn Stever, Yuki Sakurai, Nobuhiko Katayama, Aritoki Suzuki, Benjamin Westbrook, and AT Lee. Design of a testbed for the study of system interference in space cmb polarimetry. *Journal of Low Temperature Physics*, 199(3):622–630, 2020.

[63] MA Dobbs, M Lueker, KA Aird, AN Bender, BA Benson, LE Bleem, JE Carlstrom, CL Chang, H-M Cho, J Clarke, et al. Frequency multiplexed superconducting quantum interference device readout of large bolometer arrays for cosmic microwave

background measurements. *Review of Scientific Instruments*, 83(7):073113, 2012.

[64] Martin Lueker, CL Reichardt, KK Schaffer, O Zahn, Peter AR Ade, KA Aird, BA Benson, LE Bleem, JE Carlstrom, CL Chang, et al. Measurements of secondary cosmic microwave background anisotropies with the south pole telescope. *The Astrophysical Journal*, 719(2):1045, 2010.

[65] Yoichi Sato, Kenichiro Sawada, Keisuke Shinozaki, Hiroyuki Sugita, Kazuhisa Mitsuda, Noriko Y Yamasaki, Takao Nakagawa, Shoji Tsunematsu, Kiyomi Ootsuka, and Katsuhiro Narasaki. Development of 1k-class joule–thomson cryocooler for next-generation astronomical mission. *Cryogenics*, 74:47–54, 2016.

[66] HI Smith. Optical-contact bonding. *The Journal of the Acoustical Society of America*, 37(5):928–929, 1965.

[67] Takayuki Toda, Hirokazu Ishino, Kunimoto Komatsu, Tomotake Matsumura, Yuki Sakurai, and Nobuhiko Katayama. Mechanical strength and millimeter-wave transmission spectrum of stacked sapphire plates bonded by sodium silicate solution. In *Millimeter, Submillimeter, and Far-Infrared Detectors and Instrumentation for Astronomy X*, volume 11453, pages 788–799. SPIE, 2020.